

New pulsar rotation measures and the Galactic magnetic field

A. Noutsos¹, S. Johnston², M. Kramer¹ and A. Karastergiou³

¹ *University of Manchester, Jodrell Bank Observatory, Macclesfield, Cheshire, SK11 9DL.*

² *Australia Telescope National Facility, CSIRO, P.O. Box 76, Epping, NSW 1710, Australia.*

³ *Astrophysics, University of Oxford, Denys Wilkinson Building, Keble Road, Oxford OX1 3RH, UK*

9 November 2021

ABSTRACT

We measured a sample of 150 pulsar Rotation Measures (RMs) using the 20-cm receiver of the Parkes 64-m radio telescope. 46 of the pulsars in our sample have not had their RM values previously published, whereas 104 pulsar RMs have been revised. We used a novel quadratic fitting algorithm to obtain an accurate RM from the calibrated polarisation profiles recorded across 256 MHz of receiver bandwidth. The new data are used in conjunction with previously known Dispersion Measures (DMs) and the NE2001 electron-density model to study models of the direction and magnitude of the Galactic magnetic field.

1 INTRODUCTION

Magnetic fields are an integral part of nature. No physical description can be complete without considering them, whether one deals with the realm of the very small (e.g. quantised Hall effect, von Klitzing 1986) or that of the very large (e.g. cosmological magnetic fields, Zel'Dovich 1965). Hence, the study of magnetic fields is essential in understanding the universe. The birth of radio-astronomy in the 1930s allowed, amongst others, the measurement of galactic magnetic fields. The closest and most relevant to us galactic magnetic field is, of course, that of the Milky Way.

The large-scale component of the Galactic magnetic field (hereafter GMF) is intertwined with a number of interesting astrophysical processes, such as the deflection of ultra-high-energy cosmic rays (UHECRs) by the GMF (e.g. Medina Tanco et al. 1998), or the existence of star-forming regions (e.g. Novak et al. 1998). A number of observables have been employed towards mapping the GMF: e.g. Zeeman splitting of spectral lines, optical starlight polarisation and Faraday rotation of polarised radio sources. However, the main challenge that most of these methods face arises from the observer's location inside the field's physical boundaries. Faraday rotation of polarised sources exploits this fact by providing a measure of the strength and direction of the line-of-sight (*los*) component of the GMF. As was first pointed out in Lyne & Smith (1968), Faraday rotation of radio pulsars, in particular, is a powerful method for mapping the GMF. One can summarise the value of pulsars towards this goal as follows: (a) pulsars are distributed throughout the entire volume of the Galactic disc; (b) they are amongst the most polarised radio sources known; and, finally, (c) the dispersion of their pulses, given by their dispersion measure (DM), not only allows one to estimate their distance to a high accuracy, but also, when combined with their rotation

measure (RM), provides a direct way of estimating the average value of the interstellar magnetic field.

The potential of Faraday rotation as a probe to the GMF has motivated campaigns to try and measure pulsar RMs. The first such efforts, by Manchester (1972) and Manchester (1974), brought the number of determined RMs to 38. An important contribution was made by Hamilton & Lyne (1987), who measured 163 values, increasing the total number of available RMs to 185. Subsequent observations by Costa et al. (1991), Rand & Lyne (1994), Qiao et al. (1995), van Ommen et al. (1997) and Han et al. (1999) brought the total to 320. To date, the pulsar catalogue contains 554 RMs: i.e. nearly a third of the pulsars known have an RM value.

The first use of available pulsar polarisation data to map the GMF led to unequivocal evidence for a clockwise (CW) directed local field, as viewed from the Galactic north, of uniform strength $\sim 2 \mu\text{G}$ (Manchester 1972; Manchester 1974). Re-analysis of 48 pulsar RMs from the Manchester & Taylor (1977) catalogue provided the first indication for a magnetic-field reversal in the Carina-Sagittarius arm (Thomson & Nelson 1980). These finds were confirmed by the work of Lyne & Smith (1989), who also suggested an additional reversal outside the Perseus arm. As more data were being collected, the field's structure to larger distances could be explored: e.g. Rand & Lyne (1994) and Han et al. (2002) reported magnetic-field reversals in the Crux-Scutum and Norma regions.

Despite the wealth of information that observational data can provide, the sole use of pulsar RMs and DMs for the estimation of the interstellar field cannot provide sufficient information about the GMF structure: this is because the quantity RM/DM can only provide a weighted average of the parallel component of the field, with the averaging performed across the distance between pulsars. But since both

the electron density and the magnetic field are far from simple functions of azimuth and distance, inverting RM/DM to obtain \mathbf{B} is not feasible.

A possible solution is to try and fit magnetic-field models to the data and find which model is more representative of the observed RMs (see section 6). A number of authors have tried various field configurations to match the available data: e.g. Sofue & Fujimoto (1983) were amongst the first to favour a 2-arm bisymmetric-spiral model, whereas Rand & Kulkarni (1989), Rand & Lyne (1994) and Vallée (2005) fitted a concentric ring model: the latter type of model showed consistency with earlier data, but more recent observations by Han et al. (2006) contradict the model predictions, especially towards the inner Galaxy.

Despite those efforts, however, the shape of the GMF remains unclear. The main difficulties in modelling arise from (a) a short-scale, seemingly random magnetic-field component — of the same order of magnitude as the large-scale one — that causes large RM fluctuations across the entire Galactic plane (hereafter GP); (b) regional anomalies of the ISM (e.g. the Gum Nebula, the North Polar Spur), which corrupt a potentially smooth RM variation; and, in addition, (c) the pulsar distances — upon which a large portion of modelling is relied — are not certain enough, which causes discontinuities in the field direction over large longitude ranges.

In this and forthcoming publications we will study the difficulties of modelling the GMF in some detail. In this paper we will concentrate first on the measurement of new, accurate RMs in order to supplement previously sparsely sampled regions of the Galaxy. We will then examine as to whether commonly studied models of GMF are consistent with the new constraints provided by our often more precise measurements, and how they can be improved to provide a better fit to the data. A full modelling of the GMF with the full sample of available data will be undertaken in a later publication.

2 OBSERVATIONS

We observed a sample of 239 pulsars with the 20-cm H–OH receiver of the Parkes 64-m radio telescope in order to obtain a polarization database at high time resolution for all these objects. The observing session was carried out from 2006 August 24 to 27. The H–OH receiver at Parkes is equipped with two, orthogonal linear feeds that are sensitive to polarised emission with an equivalent system flux density of 43 Jy (Johnston 2002). The full Stokes profiles of each pulsar were recorded using digital correlator back end, across 256 MHz of bandwidth split in 1024 frequency channels. The wide-band correlator is capable of producing high-resolution profiles with 1024 phase bins, and more than 60% of the profiles were recorded in this mode, while the rest had 512-bin resolution. We observed each of the 239 pulsars for ~ 15 min, producing ~ 90 10-s subintegrations. In order to save disk space, we further time-averaged the data to reduce them to 15 1-min subintegrations, which we later calibrated and analysed.

3 DATA ANALYSIS

We processed all the data using the PSRCHIVE software package (Hotan et al. 2004), within which we developed new software to perform RM fitting. The raw data from the wide-band correlator first underwent a process of RFI excision and polarisation calibration. Following this, each data set was summed in time to obtain four integrated Stokes profiles for each frequency channel. One average polarisation position angle (PA) was computed per frequency channel from the Stokes parameters Q and U , summed across n phase bins i corresponding to the pulse, as:

$$\text{PA} = \frac{1}{2} \arctan \left(\frac{\sum_{i=0}^n U_i}{\sum_{i=0}^n Q_i} \right) \quad (1)$$

We computed the error of this average PA using one of the two following methods, depending on the signal-to-noise ratio of the total linear polarization $L = (\sum_{i=0}^n Q^2 + \sum_{i=0}^n U^2)^{1/2}$, given by $s/n = (1/\sqrt{n})L/\sigma_I$, where σ_I is the RMS of the total intensity. For low s/n ratios (< 10), the 1σ error on the PAs, σ_{PA} , was computed numerically using the method described in Naghizadeh-Khouei & Clarke (1993). For high s/n PAs, i.e. ≥ 10 , the PA error was computed using the formula from Everett & Weisberg (2001):

$$\sigma_{\text{PA}} = \frac{\sqrt{n} \sigma_I}{2 L} \quad (2)$$

In obtaining the average PA across the pulse per frequency channel as described above, there is a possibility that the integration of Q and U may in fact lead to a low average linear polarization and, therefore, a large error on the PA. This depends on the shape of the PA profile; integration of consecutive bins with orthogonal PAs significantly reduces the total linear polarization. While this possibility exists, we found that in our data the error on the average PA was significantly improved with respect to the errors on the PA in individual bins. These reduced errors were instrumental to good RM fits, therefore we deemed the process of averaging the PA appropriate.

3.1 The Rotation Measure from a Quadratic Fit with Wraps

The degree of Faraday rotation, ΔPA , that electromagnetic waves of wavelength λ undergo as they propagate through the interstellar medium from the pulsar to the Earth is expressed by the Rotation Measure (RM). This rotation is caused by the interaction of the radio waves with the magnetised plasma of the interstellar medium and, more specifically, the plasma electrons along the line-of-sight (*los*) to the pulsar. If n_e is the number density of the plasma electrons along a unit column of length equal to the distance to the pulsar, d , and \mathbf{B} , the magnetic field of that plasma, then RM is given as the path integral of $n_e \mathbf{B}$ along the line of sight:

$$\text{RM} = \frac{e^3}{2\pi m_e^2 c^4} \int_0^d n_e(s) \mathbf{B}(s) \cdot d\mathbf{s} \quad (3)$$

where $d\mathbf{s}$ is the path vector element in the direction of wave propagation, e is the electron charge, m_e , the electron mass and c , the speed of light. Using cgs units for the constants and expressing the distance in pc and B in μG , we get

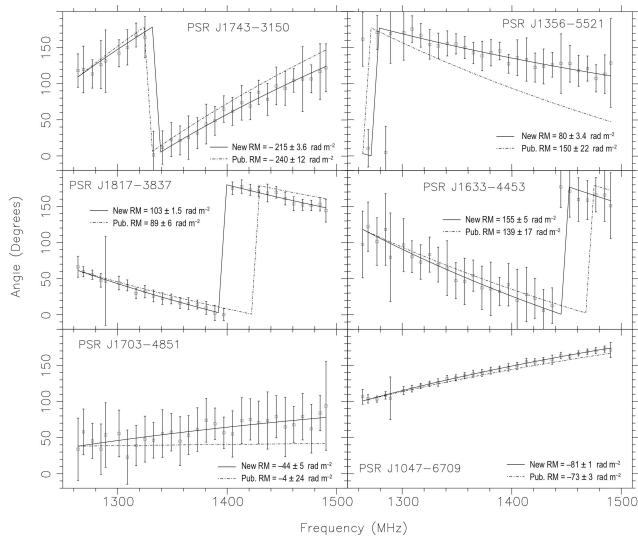


Figure 1. Examples of RM results obtained using a quadratic fit with wraps. The position angle, PA, is plotted against frequency. The solid lines represent the best fit from the method described here, whereas the dashed-dotted lines correspond to the fits based on previously published RMs by Han et al. (2006).

$$\text{RM} = 0.812 \int_0^d \left[\frac{n_e(s)}{\text{cm}^{-3}} \right] \left[\frac{\mathbf{B}(s)}{\mu\text{G}} \right] \cdot \left(\frac{ds}{\text{pc}} \right) \quad (4)$$

so that RM is expressed in the usual units of rad m^{-2} .

An observable property of the above magneto-optical interaction is that, for a particular pulsar, the longer the wave, the greater the effect of Faraday rotation, with infinitely short waves being unaffected. Mathematically, this relationship is expressed as

$$\Delta\text{PA} = \text{RM}\lambda^2 = c^2\text{RM} \frac{1}{f^2} \quad (5)$$

where f is the frequency of the waves.

Eq. 5 implies that the RM can be measured across the observation band by fitting a quadratic function to the PAs of every frequency channel. Using a Bayesian approach, we developed a fitting algorithm that was applied to the available data sets. One of the main strengths of the quadratic fitting algorithm is that it accounts for the 180° ambiguity that the PAs are subject to according to Eq. 1. The algorithm finds the best fit to the data by means of a Bayesian likelihood test. The fitting function was of the form, $\text{PA} = \text{PA}_0 + c^2\text{RM}(1/f_j^2 - 1/f_0^2)$, where PA_0 is the PA at frequency f_0 , and f_j is the frequency of channel j . The free parameters PA_0 and RM were stepped through the ranges $[0, \pi]$ rad and $[-1000, 1000]$ rad m^{-2} , in 1° and 1-rad m^{-2} steps, respectively.

The accuracy of the method is clearly displayed in the examples of Fig. 1. Our confidence in the calculated RMs is drawn both from the well calibrated data and the robust fitting approach, but also from the meticulous determination of the RM errors. The latter, we believe, has produced more firm results compared to previous efforts. The following two sections describe the procedure for the calculation of these errors.

3.2 Statistical Error on the RM from Monte Carlo Simulations

In order to estimate the statistical error on the best-fit RMs, σ_{stat} , we generated a look-up table of RM errors corresponding to the typical (average) PA error in our data, $\sigma_{\text{PA}}^{\text{data}}$, and the actual RM value that came out of the fit to the data, RM^{data} .

In order to create the look-up table, we generated Monte Carlo (MC) data sets that contained fake PA values which were calculated from a grid of chosen RM values, $\langle \text{RM}^{\text{mc}} \rangle$, using Eq. 5. The observation bandwidth and central frequency in our calculations were matched to those of the real data. The chosen grid of RM values was $\langle \text{RM}^{\text{mc}} \rangle = \{0, 5, 10, 20, 50, 100, 200, 300, 500, 800, 1000\}$ rad m^{-2} . In each Monte Carlo data set, the fake PAs were the products of randomisation of the calculated PA (from Eq. 5) within the window $[-\sigma_{\text{PA}}^{\text{mc}}, \sigma_{\text{PA}}^{\text{mc}}]$. We ranged the value of $\sigma_{\text{PA}}^{\text{mc}}$ between 1 and 63 degrees, in 1-deg steps. For each combination of $\sigma_{\text{PA}}^{\text{mc}}$ and $\langle \text{RM}^{\text{mc}} \rangle$ values, we generated 2,000 Monte Carlo data sets. Each of the generated MC data sets were then fitted using the fitting routine that was used with the real data. The resulting RM values from the fits, RM^{mc} , were Gaussian distributed around the value $\langle \text{RM}^{\text{mc}} \rangle$ that was used to generate that data set. For each distribution, we kept the RMS spread as the σ_{stat} corresponding to the particular pair of $\{\langle \text{RM}^{\text{mc}} \rangle, \sigma_{\text{PA}}^{\text{mc}}\}$ values that was used to generate the distribution.

The look-up table that was generated in this way allowed us to assign a statistical error to the RM^{data} values of the real data, given the typical $\sigma_{\text{PA}}^{\text{data}}$ of the PAs, by matching — as closely as possible — the values of $\sigma_{\text{PA}}^{\text{data}}$ and RM^{data} to those of $\sigma_{\text{PA}}^{\text{mc}}$ and $\langle \text{RM}^{\text{mc}} \rangle$. For values lying between the tabulated ones, we used a two-dimensional cubic-spline interpolation of the table values.

3.3 Systematic Error Determination

We made an effort to try and determine the systematic effects on the data, which can be caused e.g. by imperfect polarisation calibration or RFI mitigation. The procedure followed was that above, but at the start of each fitting process we averaged the number of frequency channels by a factor K_f , whose value we varied before each fit. More specifically, three different factors were used, 32, 64 and 128, which guaranteed a minimum of 8 frequency channels in the fit — thus avoiding low statistics. It is expected that increasing the value of K_f will lead to increased s/n per frequency channel; but it also means that there are fewer degrees of freedom in the fit. Thus, the resulting value of the RM should stay the same, unless there are systematic effects that alter each result. The magnitude of those systematic effects can be estimated as the bias-corrected standard deviation of those three values. Prior to this estimate, each of the values was weighted by the inverse square of the goodness-of-fit probability, p_{fit} , arising from the Bayesian fitting. Hence, we calculated the systematic error as

$$\sigma_{\text{sys}} = \sqrt{\frac{1}{2} \sum_{K_f=32}^{128} (\text{RM}_{K_f} - \langle \text{RM}_{K_f} \rangle)^2} \quad (6)$$

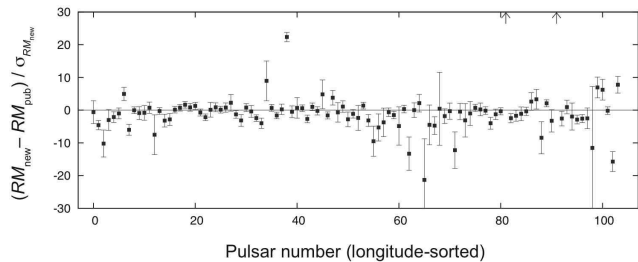


Figure 2. Residuals’ plot between previously published RMs (RM_{pub}) and those calculated from our analysis (RM_{new}), for 108 pulsars, sorted by increasing Galactic longitude (ℓ). The order number for each pulsar is shown in parentheses, in column 1 of Table 1. The RM residuals were calculated by subtracting the published from the new RM value and dividing the result by the standard deviation of the new RM. The two arrows at the top of the plot correspond to RM measurements for PSRs J1633–5015 (leftmost) and J1707–4053 (rightmost), for which the residuals were outside the plot’s range.

where $\langle RM_{K_f} \rangle$ is the weighted mean with weights equal to $w_{K_f} = 1/p_{\text{fit}}^2$.

4 RESULTS

Of the 239 pulsars in our sample, our analysis produced RM values for 150. The remaining 89 pulsars had either low s/n generally or very little linear polarization. Of the 150 RMs obtained, 46 are values measured for the first time and 104 revised from their previous values. The sample of previously unpublished RMs covers over 200° Galactic longitude and is mostly confined within a 4 kpc radius from the Sun. Apart from being a valuable addition to previous RM databases, the new sample enriches our knowledge of RMs in the first quadrant in particular ($0^\circ \leq \ell \lesssim 70^\circ$), which was previously poorly sampled. All resulting RM values and the respective combined errors ($\sigma_{\text{RM}} = (\sigma_{\text{stat}}^2 + \sigma_{\text{sys}}^2)^{1/2}$) are listed in Table 1.

Fig. 2 shows a comparison between our sample of RMs and previous results from the literature. The results agree within the error bars for the majority of the sample. Some objects show disagreement at the level of up to 10 rad m^{-2} . This could simply be due to the measurement techniques used and/or an incomplete estimate of the error bars. However, it is known that systematic changes in RM at this sort of level can occur over periods of years as the pulsar traverses through the interstellar medium (e.g. in the Vela pulsar, Johnston et al. 2005). These differences would be worth following up in more detail. A few pulsars have extremely discrepant RMs, the nature of which is not entirely clear but may be as simple as typographical errors in the original reports. In particular, the RMs of PSRs J0255–5304, J1633–5015 and J1707–4053 are wildly at odds with literature values (see Fig. 2).

5 MAGNETIC FIELD MODELLING

The value of the rotation measure for each pulsar from observations can be used to provide an estimate of the average magnitude of the component of the regular Galactic magnetic field that is directed along the los to the pulsar:

$$\langle B_{\parallel} \rangle = \frac{\int_0^d n_e(s) B_{\parallel} ds}{\int_0^d n_e(s)} \quad (7)$$

where the denominator is the column-density integral to the pulsar, called the dispersion measure, DM. Hence,

$$\langle B_{\parallel} \rangle = 1.232 \left(\frac{\text{RM}}{\text{rad m}^{-2}} \right) \left(\frac{\text{DM}}{\text{pc cm}^{-3}} \right)^{-1} \quad (8)$$

resulting in a value for B_{\parallel} in μG .

The form of the Galactic free-electron density, $n_e(s)$, is derived from modelling. In this work, we assumed the density distribution described in the NE2001 model by Cordes & Lazio (2001) — other models include e.g. the TC93 model by Taylor & Cordes (1993). Furthermore, in what follows, we will use the Galactocentric Cartesian coordinate system of the NE2001 model, shown in Fig. 10. All radii in our modelling correspond to Galactocentric distances, with the azimuth angle, θ , measured clockwise from the Galactic centre–Sun direction.

For the observed sample of pulsars, the value of $\langle B_{\parallel} \rangle$ is shown in column 6 of Table 1. Despite the fact that pulsar RMs allow us to probe only the average magnitude of the GMF along the los , the numerous, scattered pulsar positions across the Galactic disc — as well as a number of them in the Galactic halo — makes up for a powerful method to test the various theoretical models that describe its shape and magnitude.

5.1 Regular GMF models

Below are four analytical models which we chose to test for consistency against the data. The first three are described in Kachelrieß et al. (2007) and have the common component of a logarithmic-spiral disc field (first proposed by Simard-Normandin & Kronberg 1980). The last model is the pure dipolar-toroidal field (produced by an A0 dynamo), which is considered the most likely configuration for the magnetic field of the halo (e.g. Han et al. 1997, Han 2002). In the description of the spiral models, we have indicated in the subsection title whether the model has a bisymmetric spiral (BSS) or antisymmetric spiral (ASS) configuration and whether the field is antisymmetric (indicated by “-A”) or symmetric (indicated by “-S”) with respect to the GP ($z = 0$).

Previous efforts to check the consistency between the available models and the data include Han et al. (1999), who concluded that an ASS with no reversals fits well pulsars at high latitudes ($|b| > 8^\circ$), whereas the disc field can be better described using a bisymmetric-spiral configuration (BSS); a concentric-ring model (Rand & Kulkarni 1989) was the least supported by the data. Indrani & Deshpande (1999) have also tried to fit 131 pulsars to a concentric-ring and a BSS model: the latter gave the best overall fit. Nevertheless, it is worth mentioning that both models supported a stronger field in the interarm regions compared to that in the arms and that the general conclusion was that the field is reversed

Table 1. The results from the herein analysis (column 2), including the combined statistical and systematic errors (column 3). The table is sorted by the RA of each pulsar. For compatibility with Fig. 2, the ascending order according to ℓ , of pulsars with previously published RM values, is given next to each pulsar’s J2000 name (Column 1). Columns 4 and 5 show the RM values and their error that were previously published for these pulsars; the relevant publications are letter-coded, with the corresponding reference listed below the table. The last two columns, column 6 and 7, list the average value of the parallel component of the magnetic field, and its error, based on Eq. 8.

PSR	ℓ [deg]	b [deg]	DM [pc cm ⁻³]	d [kpc]	RM _{pub} [rad m ⁻²]	σ_{RM} [rad m ⁻²]	RM _{new} [rad m ⁻²]	σ_{RM} [rad m ⁻²]	B_{\parallel} [μG]	$\sigma_{B_{\parallel}}$ [μG]
J0034–0721 ⁽¹⁸⁾	110.42	–69.82	11.38	0.41	9.8 ^(a)	0.2	12.8	4	1.08	0.39
J0108–1431 ⁽¹⁹⁾	140.93	–76.81	2.38	0.2	–0.3 ^(b)	0.1	3.0	2	1.55	4.26
J0134–2937 ⁽³¹⁾	230.25	–80.25	21.81	0.56	13 ^(c)	2	15.4	3	0.79	0.15
J0151–0635 ⁽²⁰⁾	160.37	–65	25.66	1.22	2 ^(a)	4	8.1	7	0.53	0.34
J0152–1637 ⁽²²⁾	179.31	–72.46	11.92	0.51	2 ^(d)	1	–0.2	3	0.21	0.28
J0206–4028 ⁽³⁶⁾	258.60	–69.63	12.9	0.58	–4 ^(d)	5	8.8	18	0.29	1.69
J0211–8159 ⁽⁶⁰⁾	299.59	–34.61	24.36	1	54 ^(b)	9	30.0	16	1.77	0.8
J0255–5304 ⁽³⁹⁾	269.86	–55.31	15.9	0.73	–35 ^(b)	3	32.1	3	2.48	0.27
J0304+1932 ⁽²¹⁾	161.14	–33.27	15.74	0.62	–8.3 ^(e)	0.3	–7.0	1	–0.55	0.11
J0401–7608 ⁽⁵⁴⁾	290.31	–35.91	21.6	0.68	19 ^(d)	0.50	25.9	5	1.48	0.29
J0448–2749 ⁽²⁹⁾	228.35	–37.92	26.22	1.29	24 ^(b)	17	–10.9	27	1.17	1.27
J0450–1248 ⁽²⁶⁾	211.08	–32.63	37.04	1.89	13 ^(a)	5	15.5	18	1.23	0.59
J0459–0210 ⁽²⁵⁾	201.44	–25.68	21.02	0.92	18 ^(c)	9	26.9	10	1.88	0.56
J0520–2553 ⁽³⁰⁾	228.43	–30.54	33.77	1.74	19 ^(c)	15	–12.4	10	–0.22	0.36
J0525+1115 ⁽²³⁾	192.70	–13.25	79.34	3.11	37 ^(f)	2	15.3	10	0.14	0.15
J0536–7543 ⁽⁵¹⁾	287.16	–30.82	17.5	0.79	28 ^(c)	2	25.2	1	1.76	0.07
J0540–7125 ⁽⁴⁴⁾	282.15	–31.24	29.41	1.27	43 ^(c)	15	68.7	25	2.64	1.05
J0601–0527 ⁽²⁷⁾	212.20	–13.48	80.54	3.93	62.4 ^(f)	2	64.0	2	0.99	0.03
J0624–0424 ⁽²⁸⁾	213.79	–8.04	70.83	2.78	42 ^(a)	7	48.8	3	0.83	0.05
J0631+1036 ⁽²⁴⁾	201.22	0.45	125.4	3.67	137 ^(b)	8	137.5	4	1.38	0.03
J0656–2228	233.66	–8.98	32.39	1.9	–	–	38.3	12	1.9	0.45
J0719–2545	238.93	–5.83	253.89	45.32	–	–	163.6	18	0.82	0.09
J0729–1836 ⁽³²⁾	233.76	–0.34	61.29	2.9	53 ^(a)	6	51.5	4	1.01	0.09
J0738–4042 ⁽³⁴⁾	254.19	–9.19	160.8	2.64	14.5 ^(g)	0.7	12.1	0.6	0.1	<0.01
J0742–2822 ⁽³³⁾	243.77	–2.44	73.78	2.07	149.95 ^(c)	0.05	148.5	0.6	2.47	0.01
J0745–5353 ⁽³⁸⁾	266.63	–14.27	122.3	0.25	–72 ^(d)	5	–71.0	4	–0.73	0.04
J0749–4247 ⁽³⁵⁾	257.07	–8.35	104.59	0.25	80 ^(b)	30	124.8	5	1.51	0.06
J0835–4510 ⁽³⁷⁾	263.55	–2.79	67.99	0.29	31.38 ^(h)	0.01	30.4	0.6	0.54	0.01
J0838–2621	248.81	8.98	116.9	2.63	–	–	86.1	13	0.97	0.14
J0843–5022	268.50	–4.90	178.47	0.26	–	–	155.5	23	1.02	0.16
J0849–6322	279.43	–12.17	91.29	3.25	–	–	–124.8	15	–1.86	0.21
J0905–5127 ⁽⁴⁰⁾	271.63	–2.85	196.43	3.29	292 ^(b)	3	291.0	2	1.83	0.01
J0907–5157 ⁽⁴¹⁾	272.15	–3.03	103.72	0.93	–24 ^(d)	3	–23.3	1	–0.29	0.02
J0941–5244 ⁽⁴²⁾	276.45	0.09	157.94	3.14	–243 ^(b)	4	–230.5	21	–2	0.16
J1012–5857 ⁽⁴⁵⁾	283.71	–2.14	383.9	7.93	74 ^(b)	6	72.2	8	0.23	0.03
J1017–5621	282.73	0.34	439.1	8.98	–	–	364.9	7	1.04	0.02
J1036–4926 ⁽⁴³⁾	281.52	7.73	136.53	3.98	–11 ^(c)	6	–38.0	10	–0.34	0.09
J1038–5831 ⁽⁴⁸⁾	286.28	–0.02	72.74	1.91	–53 ^(d)	20	–15.0	10	–0.22	0.18
J1046–5813 ⁽⁵⁰⁾	287.07	0.73	240.2	4.37	125 ^(b)	10	132.7	7	0.69	0.04
J1047–3032	273.49	25.13	52.54	2.37	–	–	–36.9	23	–1.13	0.54
J1047–6709 ⁽⁵⁵⁾	291.31	–7.13	116.16	2.88	–73 ^(b)	3	–79.3	2	–0.86	0.02
J1057–5226 ⁽⁴⁷⁾	285.98	6.65	30.1	0.72	47.2 ⁽ⁱ⁾	0.8	44.0	2	1.84	0.07
J1110–5637 ⁽⁵³⁾	289.28	3.53	262.56	5.62	426 ^(b)	11	418.9	3	1.96	0.01

- a. Hamilton & Lyne (1987),
- b. Han et al. (2006),
- c. Han et al. (1999),
- d. Qiao et al. (1995),
- e. Manchester (1974),
- f. Johnston et al. (2005),
- g. van Ommen et al. (1997),
- h. Hamilton et al. (1977),
- i. Taylor et al. (1993),
- j. Costa et al. (1991),
- k. Rand & Lyne (1994)

Table 1. Continued

PSR	ℓ [deg]	b [deg]	DM [pc cm ⁻³]	d [kpc]	RM _{pub} [rad m ⁻²]	σ_{RM} [rad m ⁻²]	RM _{new} [rad m ⁻²]	σ_{RM} [rad m ⁻²]	B_{\parallel} [μG]	$\sigma_{B_{\parallel}}$ [μG]
J1112–6613 ⁽⁵⁶⁾	293.19	–5.23	249.3	6.48	–94 ^(b)	18	–132.0	4	–0.65	0.02
J1123–4844 ⁽⁵²⁾	288.30	11.61	92.92	2.86	–7 ^(c)	5	–13.7	6	–0.12	0.07
J1133–6250 ⁽⁵⁷⁾	294.21	–1.30	567.8	12.1	880 ^(b)	24	848.3	6	1.84	0.01
J1137–6700 ⁽⁵⁹⁾	295.79	–5.17	228.04	5.7	–1 ^(b)	13	–11.0	16	0.02	0.09
J1141–3107 ⁽⁴⁶⁾	285.75	29.39	30.77	1.21	–60 ^(b)	30	–26.1	7	–1.08	0.28
J1141–3322 ⁽⁴⁹⁾	286.59	27.27	46.45	1.91	–33 ^(b)	14	–36.4	5	–0.98	0.12
J1146–6030 ⁽⁵⁸⁾	294.98	1.34	111.68	2.35	10 ^(b)	17	–4.9	4	–0.04	0.04
J1159–7910 ⁽⁶²⁾	300.41	–16.55	59.24	1.91	–11 ^(b)	9	–6.0	15	0.21	0.32
J1225–6408 ⁽⁶¹⁾	300.13	–1.41	415.1	10.46	356 ^(b)	23	336.6	4	0.99	0.01
J1231–4609	299.38	16.57	76	2.51	–	–	–19.9	6	–0.31	0.09
J1236–5033	300.58	12.25	105.02	3.12	–	–	49.2	13	0.48	0.16
J1240–4124	300.69	21.41	44.1	1.52	–	–	15.1	13	0.75	0.36
J1253–5820 ⁽⁶³⁾	303.20	4.53	100.58	2.16	31 ^(c)	5	17.7	1	0.21	0.01
J1305–6455 ⁽⁶⁴⁾	304.41	–2.09	505	12.13	–420 ^(j)	10	–420.0	5	–1.03	0.01
J1306–6617 ⁽⁶⁵⁾	304.46	–3.46	436.9	12.38	387 ^(b)	10	395.6	4	1.11	0.01
J1319–6056 ⁽⁶⁶⁾	306.31	1.74	400.94	7.85	–238 ^(d)	25	–280.6	2	–0.86	0.01
J1320–3512	309.54	27.29	16.42	0.68	–	–	–7.8	2	–0.53	0.13
J1320–5359 ⁽⁶⁸⁾	307.30	8.64	97.6	2.34	160 ^(j)	10	141.1	4	1.78	0.05
J1326–5859 ⁽⁶⁹⁾	307.50	3.56	287.3	6.42	–580 ^(j)	10	–579.6	0.9	–2.48	<0.01
J1327–6301 ⁽⁶⁷⁾	306.97	–0.43	294.91	5.26	96 ^(b)	12	87.0	2	0.36	0.01
J1333–4449	310.77	17.40	44.3	1.38	–	–	–71.5	17	–1.45	0.48
J1338–6204 ⁽⁷⁰⁾	308.37	0.31	640.3	9.81	–452 ^(d)	8	–459.3	4	–0.89	0.01
J1339–4712	311.42	14.87	39.9	1.22	–	–	17.0	11	0.56	0.34
J1340–6456	308.05	–2.56	76.99	1.7	–	–	–37.1	23	–0.29	0.37
J1352–6803	308.61	–5.87	214.6	5.42	–	–	30.0	7	0.14	0.04
J1356–5521 ⁽⁷²⁾	312.20	6.34	174.17	4.19	150 ^(b)	22	101.1	4	0.71	0.03
J1403–7646	307.10	–14.49	100.6	3.26	–	–	94.6	16	1.02	0.19
J1410–7404	308.35	–12.04	54.24	1.53	–	–	–3.6	4	–0.05	0.1
J1413–6307 ⁽⁷¹⁾	312.05	–1.72	121.98	2.34	45 ^(b)	9	43.8	4	0.42	0.04
J1507–4352 ⁽⁷⁸⁾	327.34	12.46	48.7	1.34	–33 ^(b)	4	–34.0	7	–0.73	0.18
J1507–6640	315.86	–7.30	129.8	3.56	–	–	–40.0	13	–0.3	0.12
J1512–5759 ⁽⁷³⁾	320.77	–0.11	628.7	7.35	513 ^(b)	16	510.0	7	1	0.01
J1514–4834	325.87	7.84	51.5	1.31	–	–	18.1	14	0.81	0.34
J1517–4356	328.85	11.46	87.78	2.23	–	–	1.0	19	–0.22	0.27
J1522–5829 ⁽⁷⁴⁾	321.63	–1.22	199.9	3.43	–18 ^(d)	10	–24.2	2	–0.15	0.01
J1528–4109	332.11	12.67	89.5	2.63	–	–	25.1	8	0.33	0.11
J1534–5405	325.46	1.48	190.82	3.37	–	–	–69.5	12	–0.36	0.08
J1535–4114	333.18	11.82	66.28	1.95	–	–	17.7	2	0.32	0.04
J1536–3602	336.55	15.84	96	3.16	–	–	–23.8	9	–0.4	0.12
J1539–5626 ⁽⁷⁵⁾	324.62	–0.81	175.88	3.13	–16 ^(d)	7	–18.0	2	–0.13	0.01
J1557–4258 ⁽⁸³⁾	335.27	7.95	144.5	4.59	–37 ^(c)	2	–41.9	2	–0.35	0.02
J1600–5751 ⁽⁷⁶⁾	325.97	–3.70	176.55	3.49	–131 ^(b)	8	–117.9	18	–0.96	0.12
J1603–5657 ⁽⁷⁷⁾	326.88	–3.31	264.07	5.14	27 ^(c)	5	27.7	3	0.12	0.01
J1605–5257 ⁽⁷⁹⁾	329.73	–0.48	35.1	1.21	9 ^(d)	3	1.0	2	0.04	0.06
J1611–5209 ⁽⁸⁰⁾	330.92	–0.48	127.57	4.35	–72 ^(b)	6	–78.3	5	–0.74	0.05
J1614–3937	340	8.21	152.44	3.79	–	–	133.0	16	1.13	0.13
J1614–5048 ⁽⁸¹⁾	332.21	0.17	582.8	7.94	–451 ^(b)	2	–452.7	5	–0.95	0.01
J1615–5537	329.04	–3.46	124.48	2.41	–	–	–53.8	16	–0.55	0.16
J1630–4733 ⁽⁸⁴⁾	336.40	0.56	498	5.65	–338 ^(b)	8	–348.2	6	–0.86	0.01
J1633–4453 ⁽⁸⁸⁾	338.73	1.98	474.1	7.12	139 ^(b)	17	159.0	6	0.4	0.01
J1633–5015 ⁽⁸²⁾	334.70	–1.57	398.41	5.68	307 ^(d)	12	406.1	2	1.26	0.01
J1637–4553 ⁽⁸⁶⁾	338.48	0.76	193.23	3.16	12 ^(b)	4	10.2	5	0.05	0.03
J1639–4604 ⁽⁸⁷⁾	338.50	0.46	258.91	3.76	–60 ^(b)	30	–28.3	12	–0.13	0.06
J1640–4715 ⁽⁸⁵⁾	337.71	–0.44	591.7	6.48	–398 ^(b)	22	–411.3	12	–0.86	0.02
J1641–2347	355.83	14.71	27.7	1.01	–	–	–22.2	4	–1.02	0.17

Table 1. Continued

PSR	ℓ [deg]	b [deg]	DM [pc cm ⁻³]	d [kpc]	RM _{pub} [rad m ⁻²]	σ_{RM} [rad m ⁻²]	RM _{new} [rad m ⁻²]	σ_{RM} [rad m ⁻²]	B_{\parallel} [μG]	$\sigma_{B_{\parallel}}$ [μG]
J1646–4346 ⁽⁹⁰⁾	341.11	0.97	490.4	5.79	–62 ^(b)	7	–24.2	18	–0.11	0.04
J1650–1654	2.86	17.23	43.25	1.47	–	–	7.2	14	0.54	0.41
J1651–7642	315.15	–19.95	80	2.99	–	–	54.1	6	0.8	0.1
J1652–1400	5.60	18.58	49.5	1.71	–	–	–49.0	10	–1.24	0.24
J1653–3838 ⁽⁹³⁾	345.88	3.27	207.2	3.66	–74 ^(b)	6	–81.7	3	–0.47	0.02
J1655–3048	352.24	7.88	154.3	3.82	–	–	–63.1	10	–0.51	0.08
J1700–3312 ⁽⁹⁷⁾	351.06	5.49	166.97	3.62	–15 ^(c)	3	–25.3	4	–0.18	0.03
J1701–3726 ⁽⁹⁵⁾	347.76	2.83	303.4	5.17	–602 ^(b)	8	–605.9	2	–2.46	0.01
J1701–4533 ⁽⁹¹⁾	341.36	–2.18	526	9.71	17 ^(b)	13	4.0	4	0.01	0.01
J1703–4851 ⁽⁸⁹⁾	338.99	–4.51	150.29	2.99	–4 ^(b)	24	–46.2	5	–0.36	0.04
J1705–1906 ⁽³⁾	3.19	13.03	22.91	0.88	–9 ^(a)	4	–19.2	1	–1.08	0.06
J1707–4053 ⁽⁹²⁾	345.72	–0.20	360	4.49	–207 ^(d)	25	168.2	4	0.56	0.01
J1717–5800	332.67	–11.48	125.22	3.47	–	–	39.0	20	0.5	0.2
J1719–4006 ⁽⁹⁴⁾	347.65	–1.53	386.6	5.13	–234 ^(b)	31	–217.9	17	–0.73	0.05
J1721–3532 ⁽⁹⁹⁾	351.69	0.67	496	5.62	205 ^(d)	75	158.9	4	0.4	0.01
J1722–3632 ⁽⁹⁶⁾	350.93	0	416.2	4.35	–307 ^(b)	8	–332.8	9	–0.96	0.03
J1733–2228 ⁽⁶⁾	4.03	5.75	41.14	1.17	–9 ^(a)	4	–12.0	3	–0.33	0.1
J1733–3716 ⁽⁹⁸⁾	351.58	–2.28	153.5	2.8	–330 ^(b)	6	–335.0	2	–2.68	0.02
J1737–3555	353.17	–2.27	89.41	1.76	–	–	50.0	4	0.7	0.06
J1739–1313	12.79	9.30	58.2	1.61	–	–	34.1	2	0.74	0.05
J1740–3015 ⁽¹⁰³⁾	358.29	0.24	152.15	2.73	–157 ^(k)	2	–168.0	0.7	–1.36	0.01
J1742–4616	344.79	–8.46	115.96	2.69	–	–	–37.9	6	–0.39	0.07
J1743–3150 ⁽¹⁰¹⁾	357.30	–1.15	193.05	3.31	–240 ^(b)	12	–215.0	4	–1.37	0.02
J1743–4212	348.38	–6.46	131.94	2.87	–	–	–20.5	6	–0.16	0.05
J1749–3002 ⁽¹⁰⁴⁾	359.46	–1.24	509.4	5.83	–313 ^(d)	7	–289.7	3	–0.7	0.01
J1750–3157 ⁽¹⁰²⁾	357.98	–2.52	206.34	3.82	111 ^(b)	8	108.6	14	0.72	0.08
J1757–2421 ⁽⁷⁾	5.28	0.05	179.45	4.4	–9 ^(b)	9	15.9	5	0.1	0.03
J1801–2920 ⁽¹⁾	1.44	–3.25	125.61	2.77	–60 ^(d)	10	–61.8	3	–0.6	0.03
J1803–2712 ⁽⁴⁾	3.49	–2.53	165.5	3.38	–147 ^(d)	18	–165.0	6	–1.22	0.04
J1805–0619	21.99	7.22	146.22	3.98	–	–	82.4	14	0.69	0.12
J1808–0813 ⁽¹²⁾	20.63	5.75	151.27	3.76	73 ^(c)	7	76.8	5	0.63	0.04
J1808–3249	359.04	–6.11	147.37	3.64	–	–	289.4	6	2.46	0.05
J1811–0154	26.61	8.03	148.1	4.44	–	–	46.5	11	0.42	0.09
J1817–3837 ⁽¹⁰⁰⁾	354.68	–10.41	102.85	2.51	89 ^(b)	6	102.9	2	1.23	0.02
J1820–1818 ⁽¹¹⁾	13.20	–1.72	436	7.04	–60 ^(b)	24	–69.8	12	–0.18	0.03
J1822–2256 ⁽⁸⁾	9.35	–4.37	121.2	2.99	142 ^(d)	4	124.0	3	1.26	0.03
J1835–1106	21.22	–1.51	132.68	2.83	–	–	42.3	3	0.4	0.02
J1837–0045	30.67	2.75	86.98	2.48	–	–	130.3	17	1.98	0.23
J1837+1221	42.41	8.74	100.6	3.91	–	–	172.9	24	2.13	0.3
J1837–1837	14.81	–5.50	100.74	2.73	–	–	137.8	8	1.63	0.1
J1852–2610 ⁽⁹⁾	9.46	–11.92	56.81	1.75	–21 ^(c)	1	–21.2	4	–0.48	0.08
J1901–0906 ⁽¹³⁾	25.98	–6.44	72.68	2.13	44 ^(c)	12	29.0	2	0.51	0.03
J1901–1740	18.14	–10.07	24.4	0.95	–	–	62.8	33	1.11	1.66
J1904+0004 ⁽¹⁶⁾	34.45	–2.81	233.61	5.74	306 ^(b)	9	289.0	6	1.53	0.03
J1919+0134	37.58	–5.56	191.9	6.17	–	–	47.0	4	0.3	0.02
J1932–3655 ⁽²⁾	2.07	–23.55	59.88	2.09	6 ^(c)	3	–7.7	3	–0.14	0.07
J1943+0609	44.47	–8.64	70.76	3.02	–	–	–11.1	15	–0.26	0.26
J2006–0807 ⁽¹⁵⁾	34.10	–20.30	32.39	1.23	–52 ^(a)	5	–61.6	3	–2.32	0.13
J2038–3816 ⁽⁵⁾	3.85	–36.74	33.96	1.36	68 ^(b)	18	38.4	14	1.49	0.5
J2048–1616 ⁽¹⁴⁾	30.51	–33.08	11.46	0.56	–10 ^(a)	0.07	–10.2	0.8	–1.18	0.1
J2108–3429 ⁽¹⁰⁾	9.70	–42.16	30.22	1.21	50 ^(c)	20	39.3	12	0.98	0.51
J2346–0609 ⁽¹⁷⁾	83.80	–64.01	22.5	0.94	–5 ^(c)	1	–4.1	6	–0.33	0.3

as one crosses the boundary between the arm and interarm regions.

5.1.1 TT Model (BSS-A)

The first model we explored was based on the model of Tinyakov & Tkachev (2002) (TT). TT developed their

model primarily to explain the trajectories of UHECRs from Active Galactic Nuclei (AGN) deflected by the GMF. Its shape resembles the spiral shape of the distribution of the optical matter in the Milky Way. The magnetic field in cylin-

drical coordinates is

$$\mathbf{B} = b(r) \cos \left[\theta - \frac{1}{\tan p} \ln \left(\frac{r}{r_0} \right) \right] f(z) \times (\sin p \hat{e}_r + \cos p \hat{e}_\theta) \quad (9)$$

where p is the *pitch angle*, which describes how tightly wound the spiral arms are: the published value for this model is $p = -8^\circ$. The radius r_0 represents the Galactocentric distance along the line between the Sun and the Galactic centre (hereafter GC) to the field maximum, $|\mathbf{B}(r, 0)|$. TT express r_0 in terms of the heliocentric distance to the closest magnetic-field reversal, d_0 : $r_0 = (r_\odot + d_0) \exp(-\frac{1}{2}\pi \tan p)$, where $d_0 = -0.5$ kpc. A negative d_0 implies that the closest reversal occurs between the Sun and the GC ($\ell = 0^\circ$), whereas positive values of d_0 place the closest reversal towards the Galactic anticentre ($\ell = 180^\circ$). The functions $b(r)$ and $f(z)$ are characteristic of such “spiral” magnetic-field models and represent the radial and vertical profile of the field’s magnitude, respectively: for the TT model, $b(r > r_{\text{core}}) = b(r_\odot) \times (r_\odot/r)$, where $b(r_\odot) = 1.4 \mu\text{G}$, and $b(r \leq r_{\text{core}}) = \text{const}$, where $r_{\text{core}} = 4$ kpc. The vertical decay is given by the exponential law $f(z) = \text{sign}(z) \exp(-|z|/z_0)$, where it is typically assumed that the value for the scale height of the Galactic halo, z_0 , is 1.5 kpc.

5.1.2 HMR Model (BSS-S)

Another spiral model which we tested against our data was based on the model of Harari et al. (1999) (HMR). This model shares the same magnetic-field shape in the Galactic disc with that of the TT model but differs in the field symmetry with respect to the GP, the latter being symmetric for the HMR model.

HMR describe their spiral as somewhat less tightly wound than that of TT, with $p = -10^\circ$, whereas the first magnetic-field reversal happens at $d_0 \approx -0.5023$ kpc. The radial magnetic-field decay in this model is described by the hyperbolic-tangent law $b(r) = (3r_\odot/r) \tanh^3(r/r_{\text{core}})$, where $r_{\text{core}} = 2$ kpc. The vertical suppression in the HMR model follows the two-scale law $f(z) = 1/[2 \cosh(z/z_1)] + 1/[2 \cosh(z/z_2)]$, where the scale heights z_1 and z_2 are typically set equal to 0.3 and 4 kpc, respectively.

5.1.3 PS Model (BSS-S)

The last spiral model that we used is a variation of the BSS-S model by Prouza & Šmída (2003) (PS). The shape of the disc is identical to that described in the TT model, the only differences being the smaller halo size, with scale height $z_0 = 0.2$ kpc, and the higher field magnitude, which we normalised to $b(r_\odot) = 2 \mu\text{G}$.

In addition to the disc and halo components, PS considered a toroidal contribution, \mathbf{B}_T , in the form of circular discs either side of the GP, with the vertical profile of the field following a Lorentzian distribution:

$$\mathbf{B}_T = -\text{sign}(z) B_{T,\text{max}}(r_\odot) \times \frac{H(r_\odot - r) + H(r - r_\odot) e^{\frac{r_\odot - r}{r_\odot}}}{1 + \left(\frac{|z| - h_T}{w_T} \right)^2} (\cos \theta \hat{x} - \sin \theta \hat{y}) \quad (10)$$

where $B_{T,\text{max}}(r_\odot) = 1.5 \mu\text{G}$ is the field maximum above the GP; $h_T = 1.5$ kpc is the height of the field maximum and $w_T = 0.3$ kpc is the half-width of the Lorentzian field profile; finally, $H(x)$ is the Heaviside step function.

A final, dipolar component is added to the above two, with Cartesian components

$$\begin{aligned} B_x &= -3 \frac{\mu\text{G}}{R^3} \cos \phi \sin \phi \sin \theta \\ B_y &= -3 \frac{\mu\text{G}}{R^3} \cos \phi \sin \phi \cos \theta \\ B_z &= \frac{\mu\text{G}}{R^3} (1 - 3 \cos^2 \phi) \end{aligned} \quad (11)$$

where $R = (r^2 + z^2)^{1/2}$, $\theta = \tan^{-1}(x/y)$ and $\phi = \cos^{-1}(z/R)$ are the Galactocentric spherical coordinates; $\mu\text{G} = 123 \mu\text{G kpc}^3$ is the magnetic dipole moment. The singularity at $R = 0$ is avoided by setting $B_z = -100 \mu\text{G}$ for $R < 500$ pc.

5.1.4 Dipolar-Toroidal Model

In addition to the spiral models, we used a pure Dipolar-Toroidal magnetic field (see e.g. Han et al. 1997). The total field, which is the sum of the toroidal and the dipolar fields, is given in spherical coordinates as

$$\begin{aligned} \mathbf{B} &= \mathbf{B}_{\text{dipole}} + \mathbf{B}_{\text{toroidal}} = \\ &= \frac{m}{R^3} (2 \cos \theta \hat{e}_R + \sin \theta \hat{e}_\theta) + \text{sign}(z) \frac{n}{R} \hat{e}_\theta \end{aligned} \quad (12)$$

The parameters m and n represent the relative magnitude of the dipolar and toroidal field components, respectively, at a given point in the Galaxy, weighted by the Galactocentric distance of that point. Recent work has reported a value of $m = 245_{-56}^{+53} \mu\text{G kpc}^3$ and $n = 4.8_{-0.7}^{+0.8} \mu\text{G kpc}$ via χ^2 fitting of pulsar RMs from a sample of nearby pulsars with $d \lesssim 0.5$ kpc (Athanasiadis 2004).

Apart from the dipolar field of the PS model, none of the above model fields includes a vertical component. This is characteristic of most GMF models, although it is believed that a dipolar structure at the GC may be the reason for a weak $B_z \approx 0.2 \mu\text{G}$ at r_\odot (Han & Qiao 1994).

6 THE LARGE-SCALE STRUCTURE OF THE GALACTIC MAGNETIC FIELD REVISITED

Despite the conclusive evidence for the large-scale GMF direction within $d \sim 1$ kpc (e.g. the CW direction of the local field and the field reversal in the first quadrant (Q1) of the Sagittarius-Carina arm, Lyne & Smith 1989), past analyses of the available database of pulsar RMs have resulted in contradicting opinions with respect to the field’s structure at larger distances: Mitra et al. (2003) studied 45 pulsar RMs towards the Perseus arm and concluded that no magnetic field reversal is evident to a 5–6 kpc distance; more recently, a broader analysis of 223 southern pulsars by Han et al. concluded that the arm regions maintain a counter-clockwise (CCW) magnetic field whereas the data suggest that the field is clockwise (CW) in the interarm regions (Han et al. 2006). In addition to the usefulness of Galactic pulsars in studying the GMF, a number of authors have included extragalactic sources in their analyses.

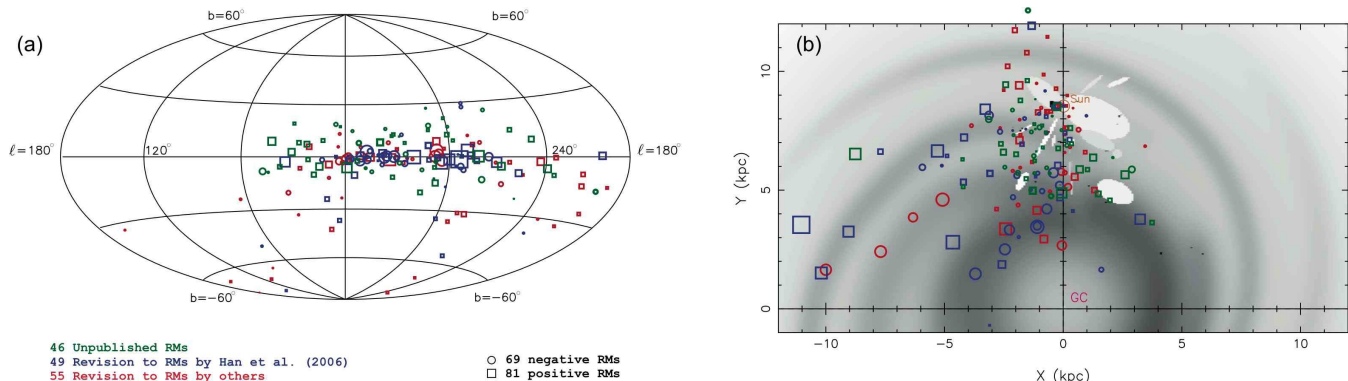


Figure 3. (a) Hammer-Aitoff (edge-on) and (b) Galactic-plane (face-on) projections of the observed sample of pulsars which were used in our analysis. The Galactic-plane projection also includes a gray-scale map of the free-electron density distribution according to the NE2001 model. The associated symbols correspond to 150 good-quality RM measurements. Each symbol’s linear dimension is proportional to $(|\text{RM}|)^{1/2}$ derived from each measurement: positive RM measurements are represented with squares; negative ones, with circles. The largest square corresponds to $\text{RM} = 848.3 \text{ rad m}^{-2}$ and the largest circle, to $\text{RM} = -605.9 \text{ rad m}^{-2}$. In addition, the plot further classifies the total sample into RMs from pulsars without a previous measurement (green), values from pulsars that had an RM recently published by Han et al. (blue), and values from pulsars with previously published RMs by other authors (red).

In 2003, Brown et al. (2003) combined 262 RMs of extragalactic radio sources from the Canadian Galactic Plane Survey (CGPS; Taylor et al. 1999) with 12 RMs of pulsars observed by Mitra et al. (2003) and others, to conclude that there are no reversals beyond the solar radius. Very recently, Brown et al. (2007) measured the RMs of 148 extragalactic radio sources from the Southern Galactic Plane Survey (SGPS; McClure–Griffiths et al. 2005) and combined them with 120 known pulsar RMs, from Han et al. (2006), Han et al. (1999) and Taylor et al. (2000), within the SGPS region ($253^\circ \leq \ell \leq 358^\circ$). They concluded that no reversals exist beyond the radius of the Sagittarius–Carina arm, in the region surveyed by the SGPS, and that the field maintains a CW direction in that region. However, they found clear evidence of a reversal in the interarm region between the Sagittarius–Carina and Scutum–Crux arms, where the field is CCW.

In order to shed more light on the problem of field reversals beyond the solar neighbourhood, we analysed the sample of 150 pulsar RMs shown in Table 1. Amongst them, there are 57 previously unpublished values that correspond to 52 pulsars, of which more than 90% are distributed within $d = 4 \text{ kpc}$, but with a longitudinal spread covering more than 200° across the sky. The longitudinal and latitudinal pulsar distribution in the sky is graphically presented in Fig. 3a, which shows a Hammer-Aitoff projection of all pulsar positions and their relative RM magnitude. Furthermore, a two-dimensional projection of the GP in Fig. 3b shows the radial distribution of the pulsars.

A straightforward method to assess the radial profile of $\langle B_{\parallel} \rangle$ is to plot its value against distance, along different lines-of-sight. According to Lyne & Smith (1989), the magnetic field in the region between distance d_1 and d_2 along the los can be assessed from the ratio of the RM and DM gradients over that region: i.e.

$$\langle B_{\parallel} \rangle_{d_1-d_2} = 1.232 \frac{\Delta \text{RM}}{\Delta \text{DM}} \quad (13)$$

Ideally, one would need an infinite number of pulsars in order to represent the actual fluctuations of $\langle B_{\parallel} \rangle_d$ with

distance, d . In practice, this method is limited by the number of pulsars lying within a solid angle of a certain longitude and latitude width, $\Delta \ell$ and Δb , respectively. However, since most pulsars in our sample lie within $|z| = 2 \text{ kpc}$ of the GP (see Fig. 4a), and because, according to the B -field models described above, the disc field does not extend beyond that z -height, it was more appropriate to plot the $\langle B_{\parallel} \rangle_d$ function inside the zone defined by $|z| \leq 2 \text{ kpc}$, instead of using a latitude constraint.

In principle, such plots can be drawn for a number of longitude sectors across the sky. One convenient way, however, to map the locations of the field reversals in a single plot is an image map of $\langle B_{\parallel} \rangle_d$, which is constructed by projecting the pulsar locations onto the Galacting plane and binning the average field values, along with the pulsar coordinates, in a polar grid (referenced at the Sun). A linear interpolation of the available field values is also introduced to smooth the GMF gradients between bins. This projection introduces an uncertainty in the z direction, which also propagates into the calculation of $\langle B_{\parallel} \rangle$ through the scale factor $\gamma = 1/(1 + (z/\rho)^2)^{1/2}$, where $\rho = (d^2 - z^2)^{1/2}$ is the polar radius. So, for a planar GMF, $\mathbf{B}(x, y)$, the projected value of the average field expressed by Eq. 7 is modified as follows as one moves away from the GP:

$$\langle B_{\parallel} \rangle = \frac{\int_0^{\gamma d} n_e(s) \gamma B_{\parallel}(s) ds}{\int_0^{\gamma d} n_e(s) ds} \quad (14)$$

where it is also assumed that the field direction does not change between the z -boundaries. Clearly, the projected field values are representative of the actual ones as long as z is chosen small enough for $\gamma \approx 1$.

6.1 Location of Reversals

Fig. 5 shows image maps, as described above, of the projected value of the parallel magnetic-field component binned along $72, 5^\circ$ longitude sectors and 1,000, 10-pc distance bins. The number of pulsars per longitude sector is distributed as

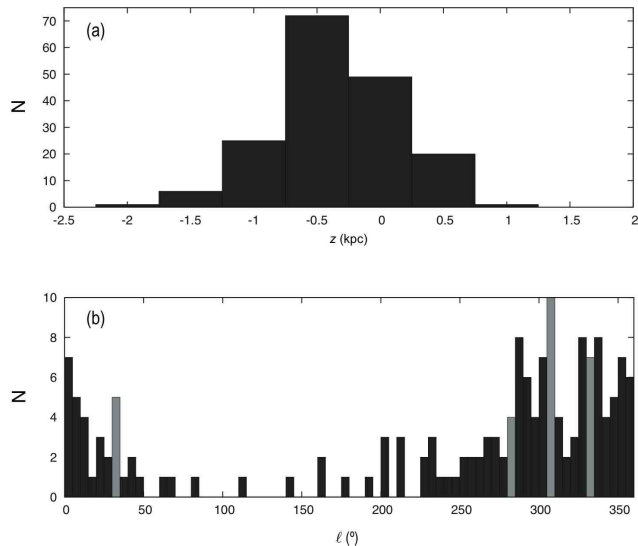


Figure 4. The distributions of (a) the z -height and (b) the Galactic longitude for the pulsar sample used in the herein analysis. The light-gray longitude bins correspond to the four 5° sectors that were checked for field reversals (see section 6.1).

shown in Fig. 4b. Only bins with available measured or interpolated data are shown: the interpolation was only possible if a bin lay between measured values; extrapolation was not performed. The different pixel intensities correspond to different values of the average field: the graduated shades of blue correspond to the range of positive GMF, i.e. directed towards the Sun, and the graduated shades of red correspond to negative GMF, i.e. directed away from the Sun. Both ends of the colour scale represent a minimum absolute value of $3 \mu\text{G}$ — meaning that stronger fields are represented by the same colour. In order to test the hypothesis of models supporting a field reversal as one crosses the GP (i.e. the class of models denoted with the suffix ‘-A’), we plotted the image maps based on (a) all available data in each sector, (b) only pulsars that lay below the GP and (c) only pulsars that lay above the GP.

6.1.1 *Crux*

One of the most evident reversals revealed by the map of Fig. 5a coincides with the *los* tangential to the Crux arm, covering 305° – 310° of Galactic longitude. The scatter plot for that sector presents a complex picture (see Fig 6a): the field is reversed from CW to CCW somewhere between the Carina and Crux arms (2–4 kpc); an increase of the field in the Crux arm region (5–10 kpc) is observed at larger distances, which however fluctuates around zero on a distance-scale of ~ 2 kpc. The field behaviour becomes less complex if one separately examines the field profiles below and above the GP (see Fig. 6b,c): in both $z > 0$ and $z < 0$ plots, the field direction between the Carina and Crux arms is CW; deep inside the Crux arm region, at ≈ 7 kpc distance, the plots for $z > 0$ reveal a second field reversal, that corresponds to a change in the field direction from CCW to CW. One has to bear in mind, of course, that the field-direction

changes were probed to only as good a resolution as the data spacing allowed.

We can compare the above statements with those of Brown et al. (2007), who provided convincing evidence for a CCW field inside the arm region, along $\ell \approx 307^\circ$. In general, our conclusions support the existence of a field with CCW direction inside the Crux arm. If we exclude the positive value at ≈ 8 kpc ($\approx 3 \mu\text{G}$), which produces a sudden reversal in the field, then the two analyses are fully compatible with a CCW field inside the arm. In addition, the presence of a reversal in the interarm region is drawn from both analyses.

Finally, we used the analytical GMF functions of section 5.1 to calculate the discrete values of $\langle B_{\parallel} \rangle_d$ at each pulsar’s position and compare it with the corresponding data value. The results are plotted with different symbols for each model in Fig. 6. In addition, the continuous profiles of the models for $z = 0$ show the fluctuation of the field along the respective sector. In general, the model values are not representative of the data and seem incapable of describing the rapid fluctuations of the field. This is perhaps an indication that the regular field component can only partly account for the observed field, whereas an additional turbulent, small-scale field is needed for the full description. For pulsars below the GP (Fig. 6b) with $d < 2$ and > 5 kpc, one can note the relatively good description of the data by the PS model.

6.1.2 *Carina*

The sector tangential to the Carina arm ($\ell = 280^\circ$ – 285°) is plotted in Fig. 6d,e,f. When all pulsars in that sector are considered, the field dips near ≈ 4 kpc to become CCW, where elsewhere it maintains a CW direction. Based on the only two pulsars below the GP, the field magnitude is decreased between ≈ 1 and 8 kpc, while maintaining a positive value. This profile is consistent with a field pattern that follows the Carina arm in a CW direction. Surprisingly, the picture is reversed for the pair of pulsars lying above the GP. The RM and DM gradients between $d \approx 4$ and 9 kpc imply a field whose magnitude increases from a very weak ($\approx -0.2 \mu\text{G}$) negative value, near 4 kpc, to a much stronger ($\approx 1.7 \mu\text{G}$) positive value, near 9 kpc, well beyond the Carina arm. This profile is indicative of a CCW field reversing to CW somewhere between 4 and 9 kpc. In comparison, Han et al. (2006) reported a CCW field in the Carina arm, but noted an evident change in the slope of $\Delta\text{RM}/\Delta\text{DM}$ between 3 and 5 kpc, which they referred to as the ‘‘Carina anomaly’’. Such a reversal, which the authors support is possibly attributed to H_{II} regions, is consistent with the profile of Fig. 6d.

Apart perhaps from the most remote pulsar in this sector, the comparison between models and data in Fig. 6a seems to favour the Dipolar–Toroidal model as the best description of the field fluctuations. Nevertheless, the model values are still more than 1 standard deviation away from the data, and furthermore the individual plots for either side of the GP show a clearly inconsistent picture between the models and the data points. A mitigating factor in this case could be the existence of H_{II} regions, which — if real — pose a clear restriction to large-scale modelling.

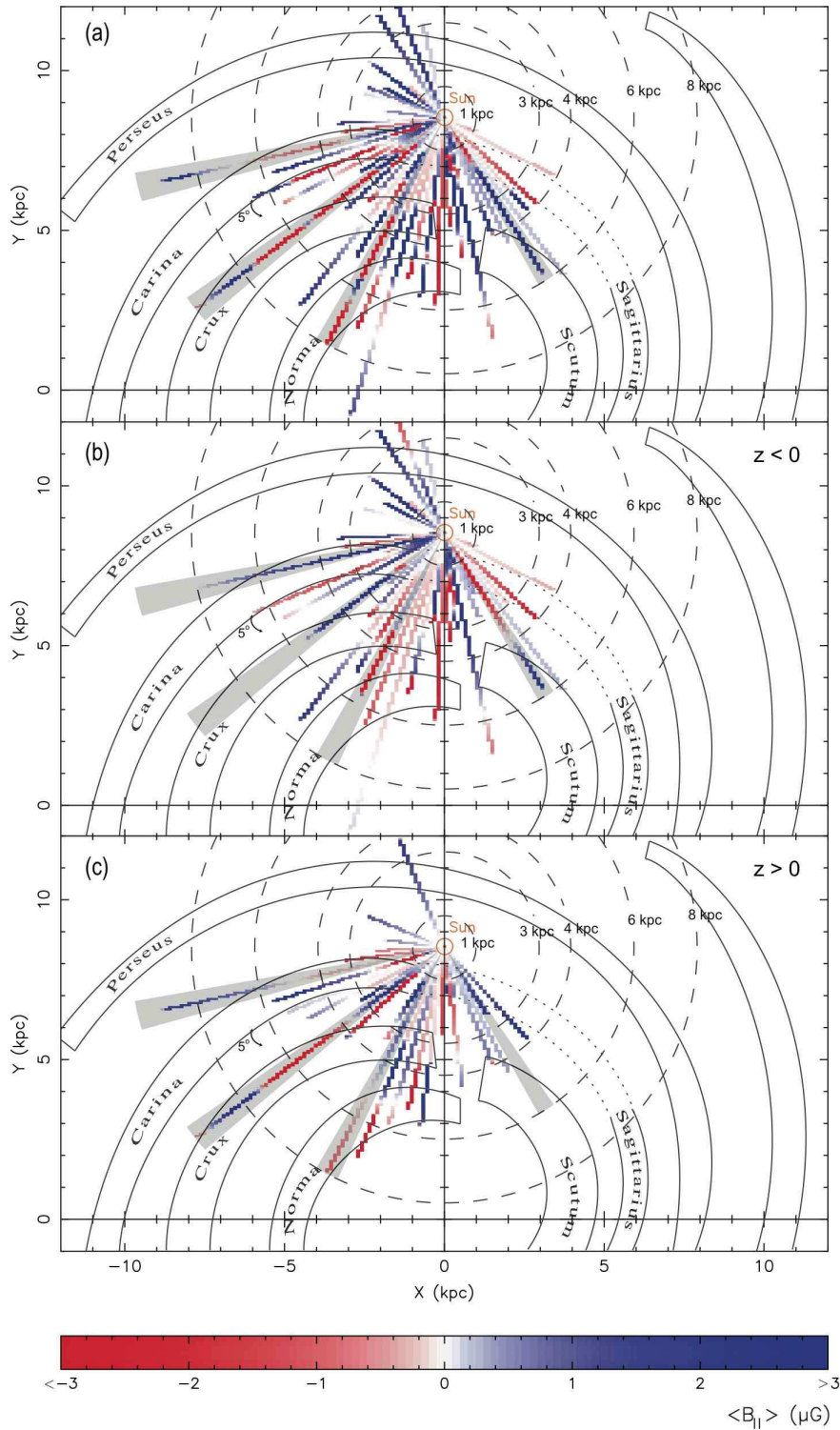


Figure 5. Image maps of the projected $\langle B_{\parallel} \rangle$ values for different longitude sectors on the GP. The field values were binned in 72, 5° longitude sectors and 1,000, 10-pc distance bins. Prior to calculating each pixel's value, based on Eq. 13, we performed a linear interpolation of the available data. Hence most pixels do not correspond to any (projected) pulsar's position. Only bins containing a value based on the above interpolation scheme are plotted, and thus each sector terminates at the location of the last pulsar available in the sector. The pixel colour and intensity along the radial paths (each representing a longitude sector of $\delta\ell = 5^\circ$) correspond to different $\langle B_{\parallel} \rangle_d$ values and are graduated from red, for fields directed away from the observer, to blue, for fields directed towards the observer, according to the scale shown below the plots. The colour scale has been intentionally saturated at both ends to reveal the field gradients in $-3 \leq \langle B_{\parallel} \rangle \leq 3 \mu\text{G}$; hence, the colour at both edges corresponds to an absolute field magnitude of at least $3 \mu\text{G}$. In order to reveal potential differences in the GMF either side of the GP, we produced the maps for (a) all pulsars, (b) those with $z < 0$ and (c) those with $z > 0$.

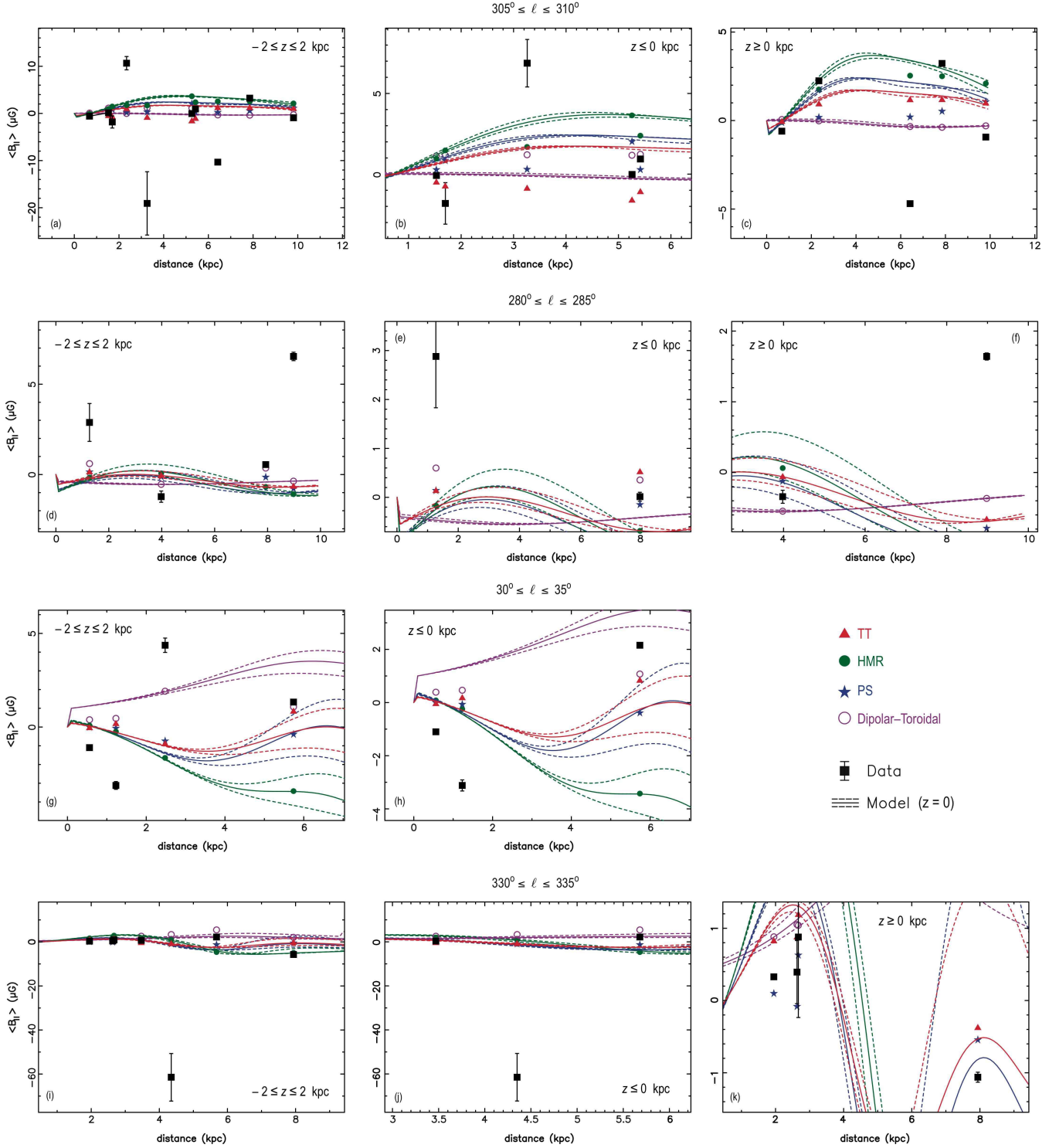


Figure 6. Scatter plots of the projected $\langle B_{\parallel} \rangle_d$ as calculated from the gradients of RM and DM between the available pulsars lying along three longitude sectors: $305^{\circ} \leq \ell \leq 310^{\circ}$ (top row), $280^{\circ} \leq \ell \leq 285^{\circ}$ (middle row) and $30^{\circ} \leq \ell \leq 35^{\circ}$ (bottom row). For each longitude sector, the field profile is shown based on the entire sample of pulsars (left column), only those that lie below the GP (middle column), and only those that lie above the GP (right column). The projection was applied to the sample of pulsars inside $-2 \leq z \leq 2$ kpc. A magnetic-field reversal in the region with $3 \leq d \leq 5$ kpc, coinciding with the far edge of the Carina–Crux interarm region, is the most likely explanation for the sudden transition from positive (field directed towards the Sun) to negative values of the projected field. Also plotted are the model values of $\langle B_{\parallel} \rangle_d$ from each model at each pulsar’s position: red triangles for the TT model, green circles for the HMR model, blue stars for the PS model and purple open circles for the Dipolar–Toroidal model. Finally, the continuous function of $\langle B_{\parallel} \rangle_d$ with distance, for each model, is plotted for $z = 0$: the solid lines correspond to the central longitude value of $\ell = 307.5^{\circ}$, and the dashed lines, to the *edges* of the longitude region.

6.1.3 Scutum

Another interesting longitude sector on the image map of Fig. 5a is the one that is tangential to the Scutum arm, between 30° and 35° . It is also a direction which was previously poorly sampled and benefited mostly from the new RMs. According to Fig. 6g, a reversal occurs between 1 and 2 kpc distance, inside the Sagittarius arm. The reversal is located near the far edge (from the Sun) of the Sagittarius arm, and it changes the field direction from CW to CCW. Fig. 6g,h seem to support a predominantly CW field in the Q1 part of the Sagittarius arm, although more pulsar RMs are needed in that region to have a solid argument. Beyond 4 kpc, this sector represents the Scutum arm, which maintains a positive value of the field, thus implying a field with a CCW direction. This result is in agreement with the findings of Han et al. (2006), who reported a CCW field across the whole of the Crux–Scutum arm. Our analysis dealt with a very limited sample of only 5 pulsars in this sector — one of which lies nominally beyond 50 kpc and was therefore excluded — and thus the available data did not allow for a better probing of the Scutum region.

Nearly all results from modelling this sector are incompatible with the observed data (see Fig. 6g,h). An exception, perhaps, are the field values from the Dipolar–Toroidal model, which weakly appear to mirror the magnetic field trend — especially for $d > 2$ kpc. However, the level of consistency is low and cannot justify giving any particular model the advantage in this case.

6.1.4 Norma

Previous studies of the field direction in the inner Galaxy have suggested that the innermost spiral arm, the Norma arm, has a CCW field across its whole extent (e.g. Han et al. 2002). As it can be seen in the maps of Fig. 5a,c, the field inside the arm (5–8 kpc) is mainly negative (apart from a very localised positive value around 6 kpc), which implies a CCW field. The picture becomes more complex in the Crux–Norma interarm region (4–5 kpc), where the field shows an abrupt, negative spike in both the plot from the total sample and that from only the pulsars below the GP. Above the GP, the region is poorly sampled and no safe conclusion can be drawn.

The “spiky” behaviour of the field’s profile, which is also seen in the Crux sector (Fig. 6a), implies magnetic fields that are an order of magnitude larger than the average value of the regular Galactic field ($\sim 2 \mu\text{G}$). The most likely explanation for such large values is a high RM gradient between pulsars, in conjunction with a small change in the electron density (see Eq. 13). This is a known phenomenon, where groups of pulsars in which the distance between pulsars is relatively short display large variations of the RM — and sometimes with a change of sign. A likely reason for such fluctuations is, again, the turbulent component of the field, which is at least as strong as the regular field (Jones 1989), while another possible reason is the presence of H_{II} regions, which can result in steep electron-density gradients, thus affecting the measured RMs.

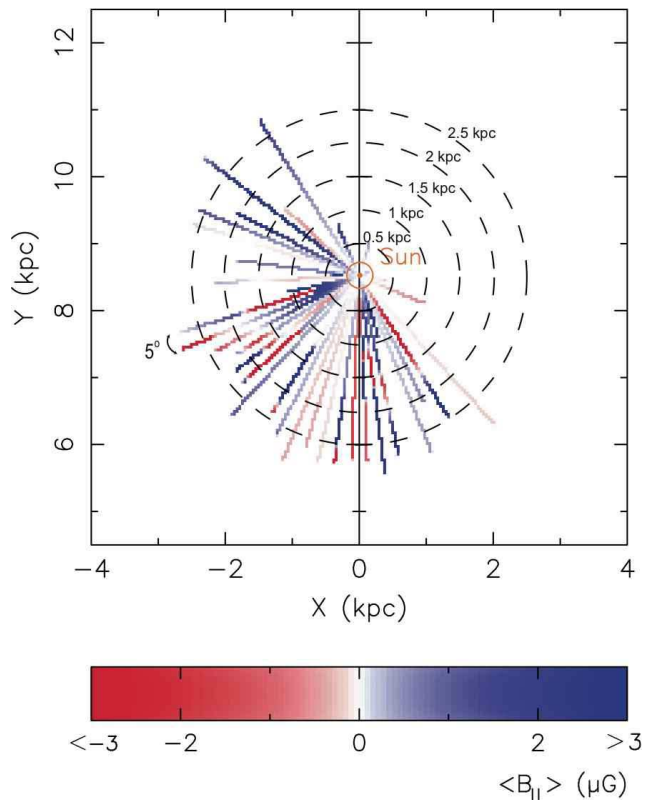


Figure 7. Image map of the projected $\langle B_{\parallel} \rangle$ values for the solar neighbourhood ($d \lesssim 2$ kpc). See Fig. 5 for details.

6.1.5 Solar Neighbourhood

The existence of reversals within the solar neighbourhood ($d \lesssim 2$ kpc) is a common conclusion of many previous studies of the GMF based on pulsar polarisation (see e.g. Lyne & Smith 1989, Dickey et al. 2001, Han et al. 2006). Fig. 7 shows an image map, similar to that of Fig. 5a, focused on the solar neighbourhood. At first glance, most longitude sectors include at least one field reversal between 1 and 2.5 kpc distance. Lyne & Smith (1989) provided evidence for a reversal between $\ell = 0^\circ$ and 70° , within $d \sim 1$ kpc. Their find can be confirmed by our image map, which shows at least one reversal between $d = 1$ and 2 kpc in the four, best-sampled sectors of that region (see Fig. 4b). Furthermore, there is evidence for a similar field pattern in Q4: Frick et al. (2001) performed a wavelet analysis that suggested a reversal in Q4, between $d = 0.6$ and 1 kpc. In that region, the only reversal in Fig. 7 is that between $\ell = 285^\circ$ and 290° . However, allowing for the large distance uncertainties borne from the uneven and coarse spacing between pulsars, one could argue that the rest of the reversals seen in that region (up to 2 kpc) support Frick’s result.

6.2 Model Refinement via Parameter Optimisation

In section 6.1, it was shown that nearly all the magnetic-field profiles along the selected longitude sectors failed to reproduce the field variation derived from actual data. This inconsistency could be partly attributed to the chosen values of the different parameters that each model depends on. It

has been known that parameter optimisation can change the model predictions from “being in dramatic disagreement with the data, to a moderately satisfying agreement” (Dickey et al. 2001).

Therefore, starting from the published parameter values for the above four models, we applied a simple fitting routine that minimises the reduced- χ^2 between the observed and model RMs. The latter were calculated via path integration along the *los* of the parallel component of the model magnetic field weighted by the NE2001 density (see Appendix for more details). For a set of n RMs and a model with two parameters, k_1 and k_2 , we can write:

$$\chi_n^2(k_1, k_2) = \frac{1}{n} \sum_{i=1}^n \frac{[\text{RM}_{\text{observed}} - \text{RM}_{\text{model}}(k_1, k_2)]^2}{\sigma_{\text{observed}}^2} \quad (15)$$

where our analysis considered all 150 RMs derived from the observations.

For multiparametric models, where the number of parameters that describe the field are $m > 2$, the fitting procedure can be performed via more than two parameters. However, the presentation of the $\chi_n^2(k_1, k_2 \dots k_m)$ map poses a plotting challenge; hence we decided to attempt to optimise only a selected pair of parameters for each model.

If one takes the published parameters for each model at face value, then the above fitting can be done through adjustment factors, ϵ and ζ , which simply translate the model-specific parameter space to dimensionless multiples of the published values: i.e. the published values correspond to $\epsilon = \zeta = 1$. We chose the fit ranges for ϵ and ζ as appropriate for each model and constructed χ_n^2 maps that helped determine the optimum pair of values for each case. The results from such fitting procedure are described in more detail below.

6.2.1 TT model

In Tinyakov and Tkachev’s model, the most obvious morphological parameters are the pitch angle, p , and the distance to the nearest field reversal to the GC, d_0 . Our fitting approach searched for an optimal value in the ranges $\epsilon : [-0.5, 3]$ and $\zeta : [0, 6]$, which correspond to the physical-parameter ranges $p = -8^\circ\epsilon : [-24^\circ, 4^\circ]$ and $d_0 = -0.5\zeta \text{ kpc} : [-3, 0] \text{ kpc}$, respectively. The resulting χ_n^2 map of that region is shown in Fig. 8a. It is clear that there is not a unique convergence to a minimum value of χ^2 for any particular pair (p, d_0) . On the contrary, the map reveals a complex dependency of the χ^2 sphere on the model parameters. It is worth noting that a number of local minima is observed, but this cannot justify their selection as representative of optimal values, as the former are randomly scattered across the map.

6.2.2 HMR model

Since the geometry of the HMR model shares many common characteristics with that of the TT model, we chose the same parameters for the χ^2 fit: i.e. the pitch angle, which was expressed as $p = -10^\circ\epsilon$, and the distance to the nearest field reversal, $d_0 \approx -0.5023\zeta \text{ kpc}$. We investigated the χ_n^2 map corresponding to a parameter space with $p : [-30^\circ, 5^\circ]$

and $d_0 : [-0.5023, 0] \text{ kpc}$. Fig. 8b shows a blown-up version of that map, focusing on the range where small values of χ^2 were found. Unfortunately, like in the case of the TT model, the resulting map appears complex and without a clear convergence. Hence, we could not optimise the HMR model’s parameters via χ^2 -fitting between the data and the model.

6.2.3 PS model

The PS model is clearly a multiparametric one, with a dipolar and a toroidal component in addition to the disc field. Focusing on the field magnitude instead of the morphology, we chose to try and find the pair of values that describe best the relative magnitude of the magnetic field in the disc compared to the toroidal one. This decision was driven by the fact that, although there is a dipolar field in this model, its planar component, $|\mathbf{B}_{\text{dipole}}(x, y)| \sim 10^{-7} - 10^{-8}$, is 5–6 times weaker than that of the toroidal field, $|\mathbf{B}_{\text{toroidal}}(x, y)| \sim 10^{-2}$; and given the fact that most pulsars considered are very close to the GP, with more than 20% of them with $|b| < 20^\circ$, the B_{\parallel} component, which is the quantity of interest, will mostly comprise the spiral and toroidal components.

Our fitting process tried to determine the absolute value of the spiral-field’s magnitude at the solar radius, $b(r_{\odot})$, and the absolute value of the toroidal field maximum, 1.5 kpc above the GP, at r_{\odot} : i.e. the value of $B_{T, \text{max}}(r_{\odot})$. For the spiral field, we expressed this as $b(r_{\odot}) = 2\epsilon \mu\text{G}$, and for the toroidal field, as $B_{T, \text{max}}(r_{\odot}) = 1.5\zeta \mu\text{G}$. The best χ_n^2 value was found in the ranges $\epsilon : [-0.5, 0]$ and $\zeta : [8, 12]$ or, in terms of magnetic field magnitude, $b(r_{\odot}) : [-1, 0] \mu\text{G}$ and $B_{T, \text{max}}(r_{\odot}) : [12, 18] \mu\text{G}$. Fig. 8c shows a contour map of that region, where the minimum χ_n^2 (≈ 3685) corresponds to $\{b(r_{\odot}), B_{T, \text{max}}(r_{\odot})\} = \{-0.35, 14.7\} \mu\text{G}$. The negative sign of the spiral field’s magnitude expresses the fact that the field direction is opposite to that assumed using the published values of Eq. 10.

6.2.4 Dipolar–Toroidal model

In the case of a pure dipolar and toroidal field, the fitting was performed on the respective distance-scaled field magnitudes expressed by the parameters m and n . Using the published values, we explored various ranges of the quantities $m = 245\epsilon$ and $n = 4.8\zeta$. The χ^2 contour map of Fig. 8d shows the region with $\epsilon : [-0.9, 0.3]$ and $\zeta : [-0.5, 2.5]$, where we found that the best-fit pair of ϵ and ζ corresponds to $\{m, n\} = \{-36.75 \mu\text{G kpc}^3, 5.37 \mu\text{G kpc}\}$ ($\chi_n^2 \approx 3516$).

Table 2 summarises the results from the successful fits of the PS and the Dipolar–Toroidal models to the data. Using the fitted values, we replotted the model predictions for the selected regions discussed in section 6.1. The results are shown in Fig. 9.

The post-fit plots show a marginal improvement on the data–model consistency. In particular, the results from the PS model appear to follow the field gradients better, although this is not the case in terms of the absolute field magnitudes. In the region of the Carina arm, for example (Fig. 9d), the post-fit results show better agreement between

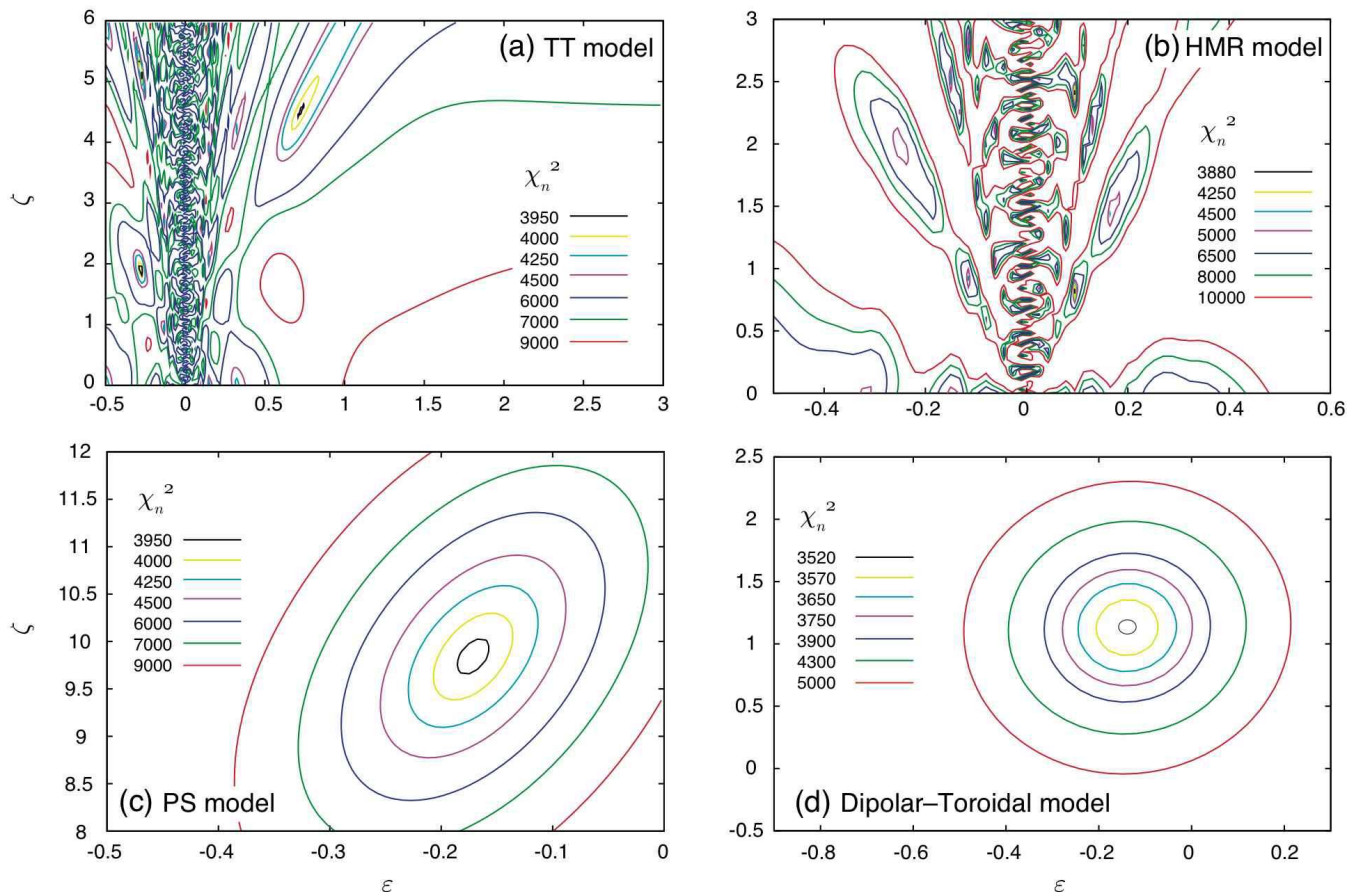


Figure 8. χ_n^2 maps of the adjustment factors, ϵ and ζ , from the parameter-fitting based on (a) the TT model, (b) the HMR model, (c) the PS model and (d) the Dipolar–Toroidal model. In all cases, ϵ and ζ multiply the published values of the physical parameters of each model: i.e. (a) $p = -8^\circ\epsilon$, the pitch angle, and $d_0 = -0.5\zeta$ kpc, the distance to the nearest field reversal from the GC; (b) $p = -10^\circ\epsilon$ and $d_0 \approx -0.5023\zeta$ kpc; (c) $b(r_\odot) = 2\epsilon$ μG , the spiral-field magnitude at the Sun, and $B_{T,\text{max}}(r_\odot) = 1.5\zeta$ μG , the maximum toroidal-field value, 1.5 kpc above the GP, at r_\odot ; (d) $m = 244.7\epsilon$ $\mu\text{G kpc}^3$, the distance-weighted toroidal-field magnitude and $n = 4.84\zeta$ $\mu\text{G kpc}$, the distance-weighted dipole-field magnitude.

the model and data points, when compared to the respective pre-fit plots. On the whole, between the two models for which the fits converged, the PS model gives the most consistent picture.

7 SUMMARY & DISCUSSION

We used our newly determined RMs to examine particular directions in the Galaxy where magnetic field reversal have been suggested. We did this by using our measurements to determine the radial profiles of the average value of the parallel component of the field along specific longitude sectors: the selected directions were those tangential to the Crux, the Carina, the Scutum and the Norma arms, and in addition an investigation of all directions within 2 kpc of the Sun were

also examined. Furthermore, we presented an overall picture of the magnetic field’s direction by means of projecting the locations of pulsars that lay close to the Galactic plane and plotting a colour-coded image map of the field direction and magnitude along 5° -longitude sectors.

Our work confirmed the existence of a field reversal in the Carina–Crux interarm region ($d = 5\text{--}10$ kpc), which has been derived from the work of Brown et al. (2007), based on extragalactic sources and pulsars. Also, a predominantly CCW field was derived from both analyses, although our work found an additional reversal near 8 kpc, deep into the Crux arm.

Furthermore, we concluded that the Carina arm maintains a CW field with the exception of a negative value at 4 kpc, which reverses the field to CCW. If this field reversal

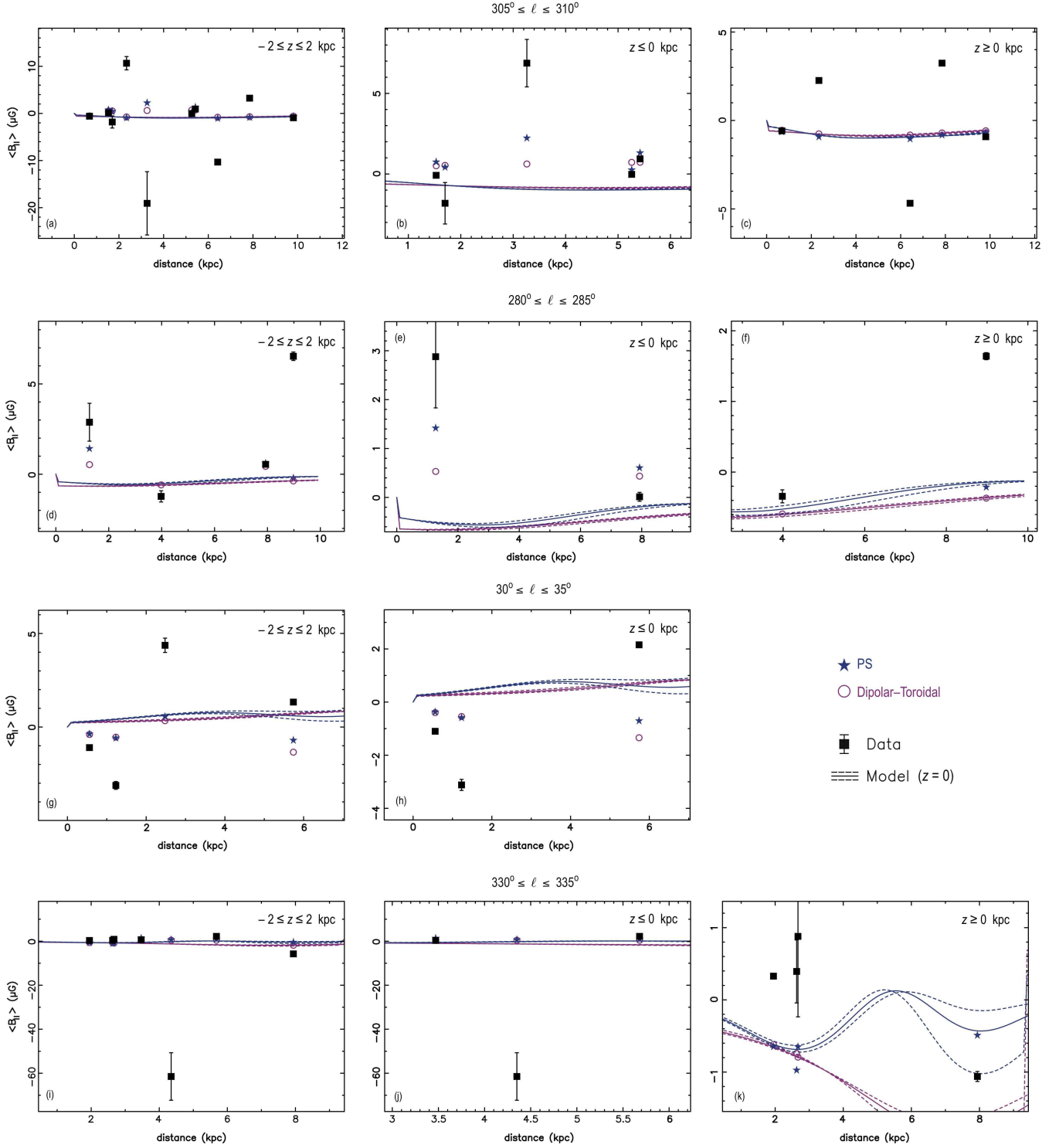


Figure 9. Scatter plots of the projected $\langle B_{\parallel} \rangle_d$ as in Fig. 6. The model parameters were adjusted according to the fitting procedure described in section 6.2.

is real, it confirms previous claims, by Han et al. (2006), of a “Carina anomaly” somewhere between 3 and 5 kpc.

Despite the poor sampling of the Galactic region tangential to the Scutum arm, beyond $d = 5$ kpc, we confirmed the existence of a CCW field, as has been previously reported. The only pulsar available in the Sagittarius–Scutum

interarm region suggests that the field direction is retained there as CCW, whereas a field reversal, at smaller distances, changes the field in the Sagittarius arm to CW.

Previous studies have indicated that the Norma arm may possess a CCW field. If this is indeed true, our findings are compatible with such field. However, it is worth noting

Table 2. The best parameter values that resulted from fitting model RMs from the PS and the Dipolar–Toroidal GMF models to $n = 150$ observed RMs. Each pair of model parameters corresponds to the minimum χ_n^2 found in a scan across the respective parameter range. The negative sign in the field magnitude implies that the field has an opposite direction to that described by the published model parameters.

		PS		Dipol.–Toroidal	
		Pub.	Opt.	Pub.	Opt.
$b(r_\odot)$	$[\mu\text{G}]$	2	−0.35		
$B_{T,\text{max}}(r_\odot)$	$[\mu\text{G}]$	1.5	14.7		
m	$[\mu\text{G kpc}^3]$			245	−36.75
n	$[\mu\text{G kpc}]$			4.8	5.37
χ_n^2			3685		3516

that we derived a CCW direction from only two pulsars with known RMs inside the arm itself.

In many of the scatter plots of the magnetic field against distance, there exist strong spikes where the field values are many times that of the expected average. This displays the vulnerability of this method to samples with neighbouring pulsars having completely different RMs.

Finally, an examination of RMs in the local neighbourhood ($d < 2$ kpc) revealed a number of reversals in Q1 and Q4. Although this reinforces the evidence for such reversals within 2 kpc, the sparse sampling prevented our analysis from determining the locations of the reversals more accurately; and, hence, it was unable to confirm results from previous, more focused studies on the region within a kpc from the Sun.

In an effort to use the new and revised RMs as a test bench for large-scale GMF modelling, we implemented a simple fitting routine. Using a selected number of existing model descriptions and the NE2001 free-electron density model, we calculated the RM predicted by these models for each of the 150 pulsars by means of integrating the electron-density-weighted model magnetic field along the line of sight to the pulsar. We found that the overall agreement of model RMs and observed data is generally poor. Even our attempts to tune key parameters of each model by a χ^2 -minimisation algorithm were only rewarded by limited success.

The difficulty to fit even a small sample of well determined RMs suggests two possibilities. On one hand, it is possible that none of the studied models actually represents the true magnetic field structure. On the other hand, small scale variations in the ISM and the GMF may alter the observed RMs sufficiently enough to cause the seen deviations from the model expectations. The success of the models to explain some of the discussed features suggest that the latter is the case. The aim must be therefore, as attempted by other authors before (e.g. Brown et al. 2007), to combine a sample of RMs as large as possible. This sample should consist of both pulsar RMs as well as those of extragalactic sources to provide calibration on the largest distances. Even then, the information may not be sufficient, and additional constraints for fitting the models should be obtained from observations other than RM measurements (see e.g. recent work by Sun et al. 2007). We will revisit such an approach in more detail in a forthcoming publication.

8 CONCLUSIONS

We used a novel technique to accurately determine rotation measures from 150 pulsars, including 46 new and 104 previously published rotation measures. Based on these values, we made an effort to investigate — and either confirm or reject — previous results on the direction of the regular Galactic magnetic field at selected regions.

We checked four models of the regular Galactic magnetic field for consistency with the data: the Tinyakov–Tkachev, the Harari–Mollerach–Roulet, the Prouza–Šmída and the Dipolar–Toroidal model. The magnetic-field values derived from all the models show large deviations from the data. After optimising the Prouza–Šmída and Dipolar–Toroidal models, for which the χ^2 fitting algorithm converged to a unique value, there was a slight improvement on the agreement between data and models. The model which benefitted mostly from the optimisation was the Prouza–Šmída model. However, the magnetic-field-magnitude inconsistencies remained at large. A probable explanation for these inconsistencies is that the models do not provide the full description of the Galactic magnetic field and that a more complete model, which will include the short-scale, turbulent Galactic-magnetic-field component, is needed. As well as lacking a short-scale component, our analysis uncovered the difficulties intertwined with the effort to fit a global magnetic field model to the data. It is almost certain that our work will be followed up with more extensive data sets and more exhaustive algorithms. However, it remains to be seen whether a successful model of the entire Galactic magnetic field is realisable. Perhaps we will have to wait until the era of the Square Kilometre Array, with its ability to obtain rotation measures for a huge number of sources, before significant further progress can be made.

REFERENCES

- Athanasiadis D., 2004, PhD thesis, University of Manchester
- Brown J. C., Haverkorn M., Gaensler B. M., Taylor A. R., Bizunok N. S., McClure-Griffiths N. M., Dickey J. M., Green A. J., 2007, *ApJ*, 663, 258
- Brown J. C., Taylor A. R., Wielebinski R., Mueller P., 2003, *ApJ*, 592, L29
- Cordes J. M., Lazio T. J. W., 2001, *ApJ*, 549, 997
- Costa M. E., McCulloch P. M., Hamilton P. A., 1991, *MNRAS*, 252, 13
- Dickey J. M., Onken C. A., McClure-Griffiths N. M., Gaensler B. M., Green A. J., Haynes R. F., Wieringa M. H., 2001, in Landecker T. L., ed., *Radio Polarization: A New Probe of the Galaxy A straw-man model of the galactic magnetic field*. DRAO, Penticton, pp 43–54
- Everett J. E., Weisberg J. M., 2001, *ApJ*, 553, 341
- Frick P., Stepanov R., Shukurov A., Sokoloff D., 2001, *MNRAS*, 325, 649
- Hamilton P. A., Lyne A. G., 1987, *MNRAS*, 224, 1073
- Hamilton P. A., McCulloch P. M., Manchester R. N., Ables J. G., Komesaroff M. M., 1977, *Nature*, 265, 224
- Han J. L., 2002, in S.Cecchini Cortiglioni S., Sault R., Sbarra C., eds, *AIP Conf. Proc. 609: Astrophysical Polarized Backgrounds Magnetic fields in our galaxy: How much do we know? (ii)*. halo field and global structure

- Han J. L., Manchester R. N., Berkhuijsen E. M., Beck R., 1997, *A&A*, 322, 98
- Han J. L., Manchester R. N., Lyne A. G., Qiao G. J., 2002, *ApJ*, 570, L17
- Han J. L., Manchester R. N., Lyne A. G., Qiao G. J., van Straten W., 2006, *ApJ*, 642, 868
- Han J. L., Manchester R. N., Qiao G. J., 1999, *MNRAS*, 306, 371
- Han J. L., Qiao G. J., 1994, *A&A*, 288, 759
- Harari D., Mollerach S., Roulet E., 1999, *Journal of High Energy Physics*, 8, 22
- Hotan A. W., van Straten W., Manchester R. N., 2004, *PASA*, 21, 302
- Indrani C., Deshpande A. A., 1999, *New Astr.*, 4, 33
- Johnston S., 2002, *Pub. of the ASA*, 19, 277
- Johnston S., Hobbs G., Vigeland S., Kramer M., Weisberg J. M., Lyne A. G., 2005, *MNRAS*, 364, 1397
- Jones T. J., 1989, *ApJ*, 346, 728
- Kachelrieß M., Serpico P. D., Teshima M., 2007, *Astroparticle Physics*, 26, 378
- Lyne A. G., Smith F. G., 1968, *Nature*, 218, 124
- Lyne A. G., Smith F. G., 1989, *MNRAS*, 237, 533
- Manchester R. N., 1972, *ApJ*, 172, 43
- Manchester R. N., 1974, *ApJ*, 188, 637
- Manchester R. N., Hobbs G. B., Teoh A., Hobbs M., 2005, *AJ*, 129, 1993
- Manchester R. N., Taylor J. H., 1977, *Pulsars*. Freeman, San Francisco
- McClure-Griffiths N. M., Dickey J. M., Gaensler B. M., Green A. J., Haverkorn M., Strasser S., 2005, *ApJS*, 158, 178
- Medina Tanco G. A., de Gouveia dal Pino E. M., Horvath J. E., 1998, *ApJ*, 492, 200
- Mitra D., Wielebinski R., Kramer M., Jessner A., 2003, *A&A*, 398, 993
- Naghizadeh-Khouei J., Clarke D., 1993, *A&A*, 274, 968
- Novak G. G., Krejny M., Li H., Chuss D. T., Calisse P. G., 2006, in *Bulletin of the American Astronomical Society* Vol. 38 of *Bulletin of the American Astronomical Society*, Continuity between Magnetic Fields in GMCs and Large-scale Galactic Magnetic Fields. pp 968–+
- Prouza M., Šmída R., 2003, *A&A*, 410, 1
- Qiao G. J., Manchester R. N., Lyne A. G., Gould D. M., 1995, *MNRAS*, 274, 572
- Rand R. J., Kulkarni S. R., 1989, *ApJ*, 343, 760
- Rand R. J., Lyne A. G., 1994, *MNRAS*, 268, 497
- Simard-Normandin M., Kronberg P. P., 1980, *ApJ*, 242, 74
- Sofue Y., Fujimoto M., 1983, *apj*, 265, 722
- Sun X. H., Reich W., Waelkens A., Enßlin T., 2007, *ArXiv e-prints*, 711
- Taylor A. R., Landecker T. L., Joncas G., eds, 1999, *New Perspectives on the Interstellar Medium* Vol. 168 of *Astronomical Society of the Pacific Conference Series*
- Taylor J. H., Cordes J. M., 1993, *ApJ*, 411, 674
- Taylor J. H., Manchester R. N., Lyne A. G., 1993, *ApJS*, 88, 529
- Taylor J. H., Manchester R. N., Lyne A. G., 2000, *VizieR Online Data Catalog*, 7189, 0
- Thomson R. C., Nelson A. H., 1980, *MNRAS*, 191, 863
- Tinyakov P. G., Tkachev I. I., 2002, *Astroparticle Physics*, 18, 165
- Vallée J. P., 2005, *AJ*, 130, 569
- van Ommen T. D., D'Alessandro F. D., Hamilton P. A., McCulloch P. M., 1997, *MNRAS*, 287, 307
- von Klitzing K., 1986, *Reviews of Modern Physics*, 58, 519
- Zel'Dovich Y. B., 1965, *Soviet Journal of Experimental and Theoretical Physics*, 21, 656

APPENDIX

Cordes & Lazio (2001) provide a FORTRAN routine to calculate the electron density, based on their NE2001 model, given a position (x, y, z) in Galactocentric coordinates. The DM calculation, when using this routine, is performed by integration of the electron density function along the *los* to a particular pulsar. Since the pulsar position, the Sun (reference) and the density function are expressed in the Galactocentric Cartesian coordinate system, the *los* has to be expressed in the same reference frame. So, the position vector \mathbf{r}_p to any point along the *los* to the pulsar is parametrised as $\mathbf{r}_p(u) = \mathbf{r}_\odot + (\mathbf{r} - \mathbf{r}_\odot)u$ (see Fig. 10). The integration path along the *los* is, therefore, expressed as $\mathbf{r}_{\text{los}}(u) = \mathbf{r}_*u = (\mathbf{r} - \mathbf{r}_\odot)u$.

Hence, the DM integral is expressed as

$$\text{DM} = \int_0^1 n_e(x, y, z) \frac{dr_{\text{los}}(u)}{du} du \quad (\text{A-1})$$

and the path integral for the calculation of RM, as

$$\begin{aligned} \text{RM} = & - \int_0^1 n_e(x, y, z) \times \\ & \times \left[B_x \frac{dx_{\text{los}}(u)}{du} + B_y \frac{dy_{\text{los}}(u)}{du} + B_z \frac{dz_{\text{los}}(u)}{du} \right] du \end{aligned} \quad (\text{A-2})$$

where the adopted analytical expression of the GMF vector, $\mathbf{B}(x, y, z)$, is taken from the models described in section 5.1.

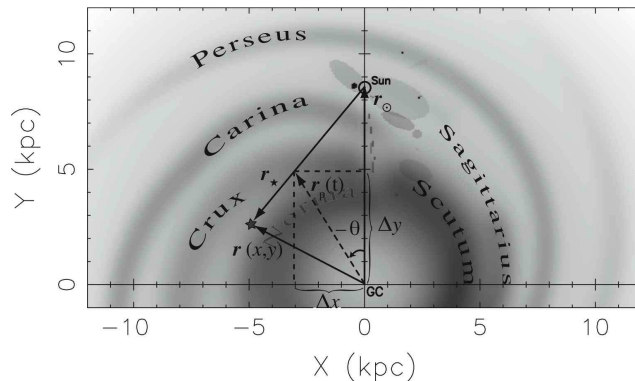


Figure 10. Schematic of the position vectors that are used in the path integration along each pulsar's *los* for the calculation of the model RMs. The coordinate system used here matches that of the NE2001 model: a right-handed Galactocentric Cartesian system, originating at the GC, and with the positive y -axis passing through the GC and the Sun. The azimuthal angle, θ , in this system increases clockwise from the GC–Sun direction.